Numerical modelling of landslide-tsunami propagation in a wide range of idealised water body geometries

Gioele Ruffini[a,*], Valentin Heller[a], Riccardo Briganti[a]

[a] *Environmental Fluid Mechanics and Geoprocesses Research Group, Faculty of Engineering, University of Nottingham, Nottingham NG7 2RD, U.K.*

Abstract

Large landslide-tsunamis are caused by mass movements such as landslides or rock falls impacting into a water body. Research of these phenomena is essentially based on the two idealised water body geometries (i) wave flume (2D, laterally confined wave propagation) and (ii) wave basin (3D, unconfined wave propagation). The wave height in 2D and 3D differs by over one order of magnitude in the far field. Further, the wave characteristics in intermediate geometries are currently not well understood. This article focuses on numerical landslide-tsunami propagation in the far field to quantify the effect of the water body geometry. The hydrodynamic numerical model SWASH, based on the non-hydrostatic non-linear shallow water equations, was used to simulate approximate linear, Stokes, cnoidal and solitary waves in 6 different idealised water body geometries. This includes 2D, 3D as well as intermediate geometries consisting of "channels" with diverging side walls. The wavefront length was found to be an excellent parameter to correlate the wave decay along the slide axis in all these geometries in agreement with Green's law and with diffraction theory in 3D. Semi-theoretical equations to predict the wave magnitude of the idealised waves at any desired point of the water bodies are also presented. Further, simulations of experimental landslide-tsunami time series were performed in 2D to quantify the effect of frequency dispersion. This process may be negligible for solitary- and cnoidal-like waves for initial landslide-tsunami hazard assessment but becomes more important for Stokes-like waves in deeper water. The findings herein significantly improve the reliability of initial landslide-tsunami hazard assessment in water body geometries between 2D and 3D, as demonstrated with the 2014 landslide-tsunami event in Lake Askja.

Keywords: Landslide-tsunamis, SWASH, diffraction theory, frequency dispersion, nonlinear waves, wave propagation

*Corresponding author
Email address: gioele.ruffini1@nottingham.ac.uk (Gioele Ruffini)

1. Introduction

1.1. Overview

Tsunamis generated by landslides are serious hazards in reservoirs (Fuchs et al., 2011; Panizzo et al., 2005), lakes (Fuchs and Boes, 2010; Gylfadóttir et al., 2017), fjords (Harbitz et al., 2014) and the sea (Watt et al., 2012; Watts et al., 2005). In this work the term "landslide" applies to mass movements such as unstable soil, rock falls, calving icebergs and snow avalanches and the term "tsunami" specifies (low frequency) waves in water bodies such as lakes, reservoirs, fjords and the sea hereafter (Liu et al., 2005).

One of the most destructive recorded landslide-tsunami was caused by an approximately 270×10^6 m^3 large landslide impacting into the Vajont reservoir in Italy in 1963. The generated wave overtopped the dam crest and flooded the valley resulting in approximately 2000 casualties (Panizzo et al., 2005). Landslide-tsunamis generated by submarine mass failures include the Papua New Guinea tsunami in 1998 where a wave of 10 m height resulted in over 2100 human losses (Synolakis et al., 2002). The 2014 landslide-tsunami in Lake Askja in Iceland is a more recent example. An approximately 20×10^6 m^3 large landslide generated a 50 m large tsunami inundating the shoreline up to 80 m (Gylfadóttir et al., 2017). On a global scale, potential landslide-tsunamis need to be assessed quite frequently considering regions such as China with over 87000 reservoirs (Liu et al., 2013), Norway with 1190 fjords (Wikipedia, 2018) and many new hydropower projects worldwide. Such past and potential future events highlight the need for reliable landslide-tsunami hazard assessment methods.

1.2. The effect of the water body geometry

Landslide-tsunamis are most reliably investigated in case specific water bodies given that the geometry and bathymetry may significantly affect the wave characteristics (Bellotti et al., 2012; Heller et al., 2012; Winckler and Liu, 2015). For generic studies, however, it is common practice to use idealised geometries. These are flume geometries (2D) and rarer basin geometries (3D) with a uniform water depth. Related geometries reflecting these idealisations can indeed be found in nature; Fig. 1a shows an example of a 2D geometry if the iceberg detaches over the entire width. The wave propagates in the direction of the main axis of the water body with the coordinate x from the landslide impact and with the water body side angles at $\theta = 0°$. Fig. 1b shows the Chahalis lake representing a 3D geometry were the waves propagate with semi-circular fronts defined with the radial distance r and a propagation angle γ from the slide impact with $\theta = 90°$.

The decay of the leading wave with distance from the landslide impact zone has been studied extensively in both 2D and 3D revealing a very different behaviour. For 2D geometries Kranzer and Keller (1959) found theoretically, that $H(x)/h \propto (x/h)^{-1/3}$, with H being the wave height and h the water depth, and laboratory experiments showed ranges between $H(x)/h \propto (x/h)^{-1/5}$ and$H(x)/h \propto (x/h)^{-0.3}$ (Heller and Hager, 2010; Heller and Spinneken, 2013;

Wiegel et al., 1970). Studies conducted in 3D found values between $H(r)/h \propto (r/h)^{-2/3}$ and $H(r)/h \propto (r/h)^{-1}$(Huber and Hager, 1997; Panizzo et al., 2005; Slingerland and Voight, 1979). According to these relationships, a wave with $H/h = 0.100$ in 2D reduces to $H = 0.034$ at $x/h = 35$, using $H(x)/h \propto (x/h)^{-0.3}$ and in 3D to 0.003 at $r/h = 35$ by using $H(r)/h \propto (r/h)^{-1}$. This over an order of magnitude difference has been confirmed experimentally by Heller and Spinneken (2015). The same authors also confirmed that the landslide-tsunami wave type changes in function of the geometry; not all of the wave types observed in 2D (commonly linked to the theoretical wave types Stokes, cnoidal, solitary and bores (Heller and Hager, 2011)) are observed in 3D.

The decay in 2D is due to two different phenomena if bottom friction is excluded; frequency dispersion (Brühl and Becker, 2018) and wave breaking which is sometimes present during tsunami generation and/or propagation. In geometries more diverging than 2D also the contribution of the lateral energy spread is present.

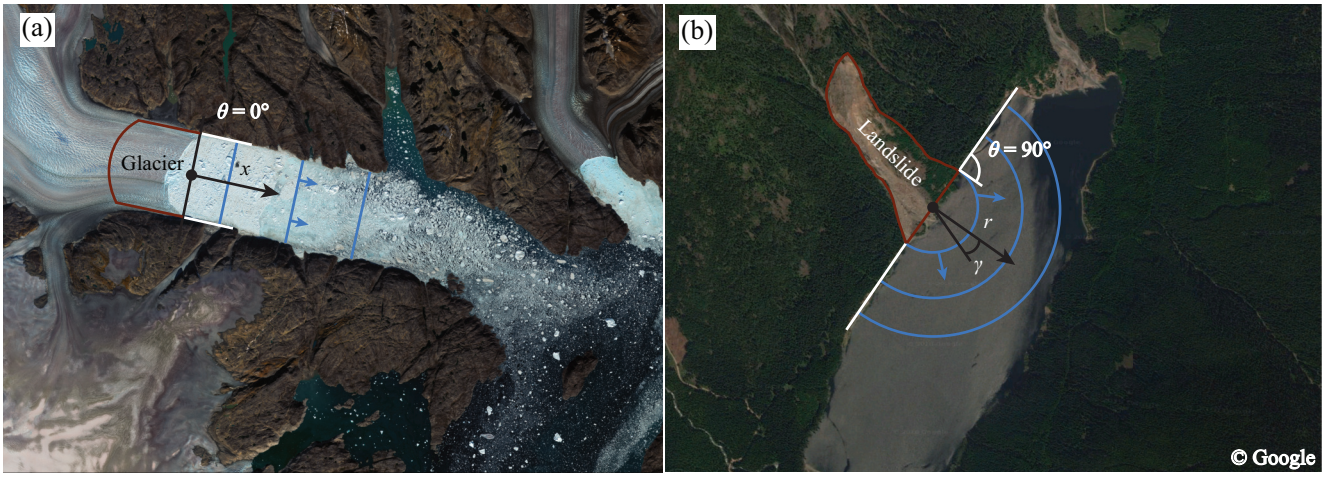

Figure 1: Landslide-tsunami settings represented by idealised geometries: (a) Heleim Glacier representing a 2D geometry (contains modified Copernicus Sentinel data, 2016, processed by Pierre Markuse) and (b) 2007 Chehalis lake case representing a 3D geometry (adapted from Google maps).

Most studies involving the effect of the water body geometry were aimed at relating landslide-tsunami parameters in 3D to 2D. Submarine landslides were investigated by Jiang and LeBlond (1994) who found that the difference between waves in 3D and 2D geometries is affected by the ratio b/l_s, where b is the slide width and l_s is the landslide length along its main axis, and Watts et al. (2005) who provide relations between tsunamis in 2D and 3D based on b and the maximum tsunami wavelength L_M.

Using subaerial landslides, Heller et al. (2009) proposed an empirical method to link the wave characteristics in 3D to 2D based on the impulse product parameter P (Heller and Hager, 2010). The wave heights H at $x/h = r/h = 5$ were thereby assumed to be identical in both geometries based on observations of Huber (1980) (follow-up research showed that this assumption is sometimes very rough, see Heller and Spinneken, 2015). Beyond this position different decays were defined for H based on Heller and Hager (2010) in 2D and Huber and Hager (1997) in 3D.

Since these studies focus all on 2D and/or 3D only, the understanding of landslide-tsunamis in intermediate geometries is limited. The pioneer study investigating an intermediate geometry was Chang et al. (1979) generating solitary waves in a flume with walls at an angle of $\theta = 1.1°$. These authors found that Green's law can be applied for $x/h < 40$. However, Green's law was found to have limited applicability for solitary and solitary-like waves for more extremely diverging flumes (Heller et al., 2012) if the width of the diverging channel is used in Green's law.

Heller et al. (2012) experimentally investigated for the first time landslide-tsunamis in different water body geometries with $\theta = 0$ (2D), $15, 30, 45, 60, 75$ and $90°$ (3D). They found that the wave heights in the far field in intermediate geometries were closer to the ones observed in 3D than in 2D. They further highlighted the need to study the effect of the water body geometry in more detail with different slide characteristics, wave types and larger water depths to avoid scale effects (Heller, 2011; Heller et al., 2008).

This was later addressed (Heller and Spinneken, 2015) with a new set of laboratory experiments in 2D and 3D with tsunamis measured up to a distance of $x/h = r/h = 35$. The authors presented a novel method to transform wave parameters (wave height, amplitude and period) from 2D to 3D for a range of block slide characteristics. Intermediate geometries with $\theta = 7.5, 15, 30$ and $45°$ were then purely numerically addressed with Smoothed Particle Hydrodynamics (SPH) (Heller et al., 2016). This provided new physical insight into the effect of the water body geometry for propagation distances $r/h \leq 7.5$. Larger distances could not be investigated due to the large computational cost of SPH.

Fig. 2 shows a scheme of the division between the wave generation and wave propagation zones of a landslide-tsunami. The wave generation zone (dashed area), with coordinate system x and (r, γ) from the slide impact, is where the momentum transfer between the landslide and water occurs (Mulligan and Take, 2017; Zitti et al., 2016). This zone is excluded from this study ensuring that the tsunamis are reasonably stable in the simulations. Two new sets of coordinate systems $x' = x + d_M$ and $(r' = r + d_M, \gamma')$ with d_M as the coupling distance (Section 3.2) are also chosen to define the wave propagation zone considered in the present study.

Herein, the landslide widths in all geometries are defined as the finite wave source width in 2D in order to relate the findings from all geometries to 2D. In 2D it is possible to quantify the effect of free components travelling with their own celerity (this process is referred hereafter as frequency dispersion) on waves generated by a landslide rather than idealised waves. Comparison with

laboratory experiments (Heller and Hager, 2011) will help to reveal this effect for each wave type. However, in the intermediate and 3D geometries this is not possible as lateral energy spread (i.e. diffraction) is present. Therefore, due to the non-linearity of the problem, it is not possible to separate the contribution of the lateral energy spread from that of frequency dispersion.

Because the wave source used is of finite width, diffraction theories (Carr and Stelzriede, 1952; Lamb, 1945; Morse and Rubenstein, 1938; Penney et al., 1952) could be used to validate the numerical simulations of this study. These theories are formulated to calculate the wave propagation of a linear wave behind a gap. This problem shows similarities with landslide-tsunamis with the slide, i.e. a wave source, of width corresponding to the gap width. Only the solution of Carr and Stelzriede (1952) is considered herein because the validity range of this theory is compatible with landslide-tsunamis ($b'/L \leq 0.5$) and it depends on both r' and γ'.

When idealised waves were considered, wave trains, rather than wave packets were simulated. This was done for two reasons: first this is more similar to actual tsunami propagation and, second, it avoids spurious numerical solutions due to propagation of isolated waves or packets in still water. Finally, this study excludes shore and other depth related effects such as reflection and depth trapping of the tsunami (Bellotti et al., 2012) and edge waves (Couston et al., 2015; Heller and Spinneken, 2015; Romano et al., 2013) which in combination with the impact on the coast may alter the tsunami characteristics.

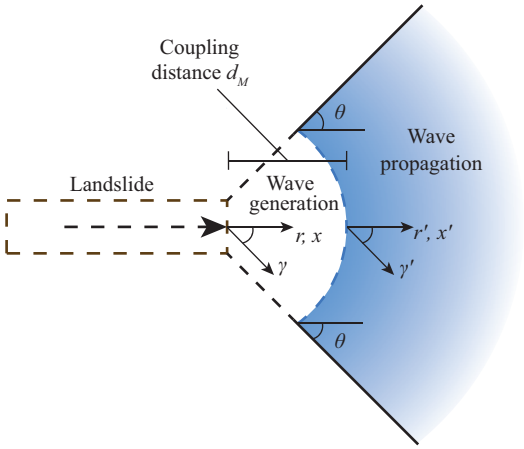

Figure 2: Scheme of the wave generation and propagation zones.

1.3. Numerical modelling

Subaerial landslide-tsunamis are challenging for numerical modelling. To overcome the difficulty in simulating wave generation and far field propagation at the same time, these two processes are usually divided using two numerical methods that are subsequently coupled (Abadie et al., 2012; Tan et al.,

2018). Suitable options for the wave propagation are NHWAVE (Ma et al., 2012), FUNWAVE-TVD (Shi et al., 2012), XBeach (Roelvink et al., 2010) and SWASH (Zijlema et al., 2011).

SWASH, which is based on the non-hydrostatic Non-Linear Shallow Water Equations (NLSWEs), was chosen in the present study. SWASH is able to simulate frequency dispersion accurately with a small number of layers (e.g. 2) by using a compact difference scheme, and can be run in parallel. SWASH has also been successfully coupled with SPH for wave propagation from off- to onshore (Altomare et al., 2015) and to study hypothetical landslide-tsunamis at Es Vedrà, offshore Ibiza (Tan et al., 2018).

1.4. Aims and structure

The present study aims to:

- Enhance the physical understanding and modelling of the effect of the water body geometry on tsunami propagation based on numerical modelling of approximate linear, Stokes, cnoidal and solitary waves in 2D, 3D and intermediate water body geometries,
- Provide insight on the effect of frequency dispersion on landslide-tsunamis,
- Provide new semi-theoretical equations accounting for the effect of the water body geometry to support landslide-tsunami hazard assessment.

The remainder of this article is organised as follows. In Section 2 the theoretical background of SWASH, the numerical setup, the boundary conditions and the calibration and validation are described. The wave propagation in idealised geometries for both idealised and real (dispersive) waves, the wave height decay and the lateral wave energy spread are presented in Section 3 along with semi-theoretical equations. In Section 4 the results are analysed and the 2014 landslide-tsunami case in Lake Askja is used as computational example. Finally, Section 5 highlights the main conclusions and future work.

2. Methodology

2.1. SWASH

SWASH v4.01 (Stelling and Duinmeijer, 2003; Stelling and Zijlema, 2003; Zijlema and Stelling, 2005; Zijlema et al., 2011) was used in the present study. Only the governing equations used to solve the equations in 2D and 3D geometries, where a regular grid is used, are presented hereafter for simplicity. For the remaining intermediate geometries the equations are solved for a curvilinear grid.

SWASH solves the depth averaged non-hydrostatic NLSWEs with the continuity and momentum equations written as

$$\frac{\partial \eta}{\partial t'} + \frac{\partial d\overline{u}}{\partial x'} + \frac{\partial d\overline{v}}{\partial y'} = 0 \tag{1}$$

$$\frac{\partial \overline{u}}{\partial t'}+\overline{u}\frac{\partial \overline{u}}{\partial x'}+\overline{v}\frac{\partial \overline{u}}{\partial y'}+g\frac{\partial \eta}{\partial x'}+\frac{1}{d}\int_{-h}^{\eta}\frac{\partial q}{\partial x'}\mathrm{d}z'+c_f\frac{\overline{u}\sqrt{\overline{u}^2+\overline{v}^2}}{d}=\frac{1}{d}\left(\frac{\partial d\tau_{x'x'}}{\partial x'}+\frac{\partial d\tau_{x'y'}}{\partial y'}\right) \tag{2}$$

$$\frac{\partial \overline{v}}{\partial t'}+\overline{u}\frac{\partial \overline{v}}{\partial x'}+\overline{v}\frac{\partial \overline{v}}{\partial y'}+g\frac{\partial \eta}{\partial y'}+\frac{1}{d}\int_{-h}^{\eta}\frac{\partial q}{\partial y'}\mathrm{d}z'+c_f\frac{\overline{v}\sqrt{\overline{u}^2+\overline{v}^2}}{d}=\frac{1}{d}\left(\frac{\partial d\tau_{y'x'}}{\partial x'}+\frac{\partial d\tau_{y'y'}}{\partial y'}\right) \tag{3}$$

where t' is the time, x', y' and z' are the coordinates located at the mean still water level (SWL), $h(x',y')$ is the still water depth, $\eta(x',y',t')$ is the water surface elevation from the SWL and $d=h+\eta$ is the total water depth. $\overline{u}$ and $\overline{v}$ are the depth-averaged flow velocities in the two main directions. $\tau_{x'x'}, \tau_{x'y'}, \tau_{y'x'}$ and $\tau_{y'y'}$ are the horizontal turbulent stresses, c_f is the bottom friction coefficient defined by Manning's formula (Zijlema et al., 2011) and g is the gravity acceleration. $q(x',y',z',t')$ is the non-hydrostatic pressure term of the total pressure p_t defined as (Zijlema and Stelling, 2005)

$$p_t = g(\eta - z') + q = p_h + q \tag{4}$$

where p_h is the hydrostatic pressure. Eqs. (1) to (3) were expanded in Stelling and Zijlema (2003) to the multi-layer case applied herein. The computation of the integral of the non-hydrostatic pressure gradient in Eqs. (2) and (3) is introduced in Zijlema et al. (2011), where the free surface boundary condition of the non-hydrostatic pressure is $q\mid_{\eta}=0$ and at the bottom it is defined by applying the Keller-Box method. Then, the vertical velocities at the free surface w_s and at the bottom w_b are introduced with the momentum equation along the vertical direction. Here, the vertical acceleration is defined at every time step from the non-hydrostatic pressure. Finally, combining the vertical momentum equations with the non-hydrostatic pressure equation at the bottom and using the kinematic bottom boundary condition $w_b=-\overline{u}\partial h/\partial x'-\overline{v}\partial h/\partial y'$, the conservation of local mass results as

$$\frac{\partial \overline{u}}{\partial x'}+\frac{\partial \overline{v}}{\partial y'}+\frac{w_s-w_b}{d}=0 \tag{5}$$

Eq. (5) closes the system of equations and allows, together with the boundary conditions, to solve Eqs. (1) to (3).

Time integration is carried out with the explicit method relying on the Courant-Friedrichs-Lewy (CFL) condition and the wave celerity that is available in SWASH. Here only the condition for 2D simulations is illustrated as the most relevant one. The Courant number C_r is defined as

$$C_r=\Delta t'\left(\sqrt{gd}+\sqrt{u^2+v^2}\right)\sqrt{\frac{1}{\Delta x'^2}+\frac{1}{\Delta y'^2}}\leq 1 \tag{6}$$

where $\Delta x'$ and $\Delta y'$ are the distances between two grid points in the x' and y' directions. To calculate the time step, a minimum and maximum C_r threshold

can be applied in the simulation in order to accurately control the convergence of the solution.

2.2. Numerical setup

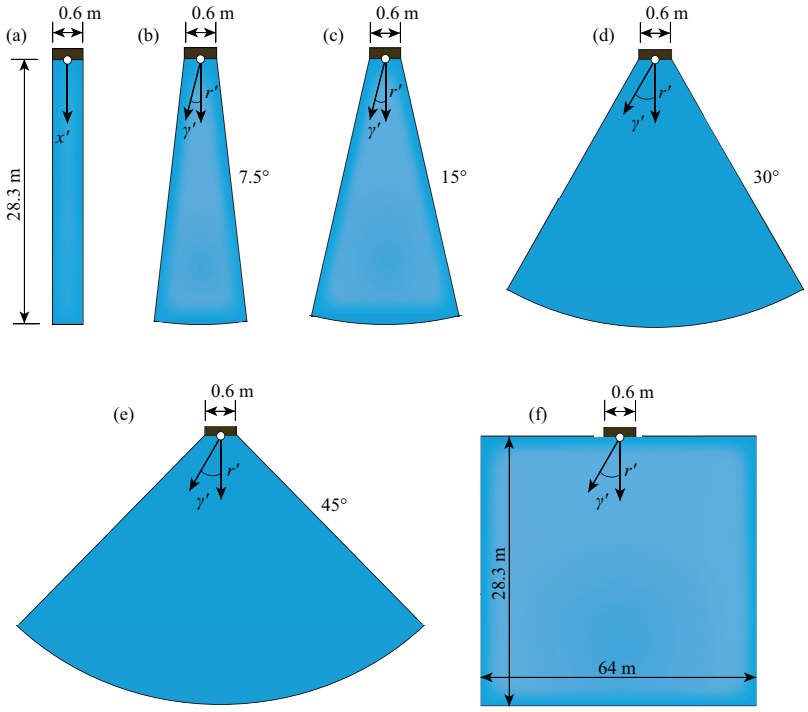

Figure 3: Investigated water body geometries in the far field modelled with SWASH: (a) 2D ($\theta = 0°$), (b) $\theta = 7.5°$, (c) $\theta = 15°$, (d) $\theta = 30°$, (e) $\theta = 45°$ and (f) 3D ($\theta = 90°$, the horizontal dimension is reduced in scale in this sketch due to lateral space constraint). The grey sections are the wave generation zones between the near and far fields.

The numerical domains used here cover the range from 2D to 3D (Fig. 3), based on the geometries used in Heller et al. (2016). The 2D geometry (Fig. 3a) consists of a 28.3 m long and 0.6 m wide flume while the 3D geometry (Fig. 3b) spans a domain of 28.3 m $\times$ 64.0 m. Intermediate geometries are defined using divergent side walls with angles of $\theta = 7.5, 15, 30$ and $45°$ (Fig. 3b-e). Geometries with $\theta > 45°$ were excluded as previous research (Heller et al., 2012; Heller and Spinneken, 2015) showed no substantial differences of the maximum wave parameters in these geometries in relation to the 3D case. The basin width of these intermediate geometries is increasing with $0.6 + (2r'\tan\theta)$ m. Each intermediate geometry was modelled with a rounded downwave boundary with radius $r' = 28.3$ m to allow for a more even distribution of the cells in this zone.

The bathymetry was flat for all investigated cases and numerical wave gauges were placed at the relative distances and angles shown in Table 1.

Table 1: Locations of the numerical wave gauges.

Geometry	Relative distance x'/h or r'/h (-)	Wave propagation angle γ' (°)
2D	3.0, 5.0, 7.5, 10.0, 15.0, 22.5, 35.0	0.0°
7.5°	3.0, 5.0, 7.5, 10.0, 15.0, 22.5, 35.0	0.0°, ±7.5°
15.0°	3.0, 5.0, 7.5, 10.0, 15.0, 22.5, 35.0	0.0°, ±7.5°, ±15.0°
30.0°	3.0, 5.0, 7.5, 10.0, 15.0, 22.5, 35.0	0.0°, ±7.5°, ±15.0°, ±22.5°, ±30.0°
45.0°	3.0, 5.0, 7.5, 10.0, 15.0, 22.5, 35.0	0.0°, ±7.5°, ±15.0°, ±22.5°, ±30.0°, ±37.5° ±45.0°
3D	3.0, 5.0, 7.5, 10.0, 15.0, 22.5, 35.0	0.0°, ±7.5°, ±15.0°, ±22.5°, ±30.0°, ±37.5° ±45.0°, ±52.5°, ±60.0°, ±67.5°, ±75.0°, ±82.5°

The 2D and 3D geometries were defined with a regular Cartesian grid while the intermediate ones were defined with an orthogonal curvilinear grid created in the RGFGRID v5.0 of the Delft3D software suite. These grids were then exported and reformatted using MATLAB to create input files readable by SWASH. The coordinate system for the grid creation was defined with $x' = 0$ at the wave generation boundary with positive values in the main wave propagation direction. The origin in the y'-direction was defined at the centre of the wave source. The wave source in all domains was 0.6 m wide. For the results, polar coordinates (r', γ') with the origin at the centre of the wave source was used, with r' as the radial distance and γ' as the wave propagation angle with the results interpolated from the grid nodes.

Furthermore, the calibration was performed using a water depth of 0.6 m in all geometries based on the experiments of Heller and Hager (2011). The numerical code was compiled with the Intel compiler 2017 and Intel-MPI libraries for the use with multiple processors using the Message Passing Interface (MPI) protocol. The model divides the computational domain in subdomains to solve the equations with multiple cores. A stripwise decomposition method along the $y'-$axis was chosen. Other methods (orthogonal recursive bisection and stripwise along the x'-direction) resulted in inconsistencies in the solutions. The University of Nottingham High Performance Computing (HPC) cluster Minerva was used to perform the simulations. A simulation time of 60 s in the 3D geometry with a grid resolution of $\Delta x' = \Delta y' = 2.5$ cm took approximately 35 hours of real time using 40 Central Processing Unit (CPU) cores and 10 GB of random access memory.

2.3. Boundary conditions

All tests for the calibration and validation of the model were performed by providing time series of linear waves as boundary conditions, allowing for a direct comparison with diffraction theory. A wave height of $H = 0.040$ m, a water depth of $h = 0.600$ m and a wave period of $T = 0.876$ s were used resulting in a wavelength of $L = 1.19$ m according to linear theory (Table 2). These conditions result in approximate linear waves. The first waves were disregarded in the analysis to include only steady wave heights.

Previous studies (e.g. Heller and Hager, 2011; Panizzo et al., 2005) showed that different slide scenarios lead to different wave types and decay characteristics. For this reason, after calibration and validation, the non-linear Stokes (Fenton, 1985), cnoidal (Fenton, 1999) and solitary waves (Boussinesq, 1872) were also reproduced and analysed herein. All wave parameters are summarised in Table 2 with a as the amplitude and c as the celerity. Bores were excluded because it is unlikely that they are observed in geometries other than 2D (Heller and Spinneken, 2015). Note that in the following the definition $H = a + a_t$ applies, which reduces for linear waves to $H = 2a$, with a_t as the wave trough. The conditions for each wave type presented in Figs. 4 (Stokes-like waves), 6 (cnoidal-like waves) and 8 (solitary-like waves) of Heller and Hager (2011) were reproduced by using the measured wave parameters in the corresponding wave theory. A time series of the water surface was calculated for each wave type and used as input for SWASH over a finite wave generation boundary $b' = 0.6$ m. The wave velocity at the boundary was solved by SWASH as previous work showed the accuracy of this approach (Ruffini et al., 2019). A ramping up function was added to smooth the initiation of the simulations to avoid numerical instabilities.

Table 2: Wave theories used in this study with the wave parameters measured in Heller and Hager (2011).

Wave theory	h (m)	H (m)	T (s)	L (m)	a (m)	c (m/s)
Linear	0.600	0.040	0.876	1.190	-	-
5^{th} order Stokes (Fenton, 1985)	0.600	0.100	1.000	1.530	-	-
5^{th} order cnoidal (Fenton, 1999)	0.300	0.155	1.740	2.830	0.110	1.630
1^{st} order solitary (Boussinesq, 1872)	0.300	0.159	-	2.823	0.159	1.969

The wave generation boundary was defined through a segment at $x' = 0$ m using a weakly reflective boundary condition (Blayo and Debreu, 2005). This formulation assumes a wave direction perpendicular to the boundary with an incident velocity $\bar{u}_i$ defined by

$$\bar{u}_i = \pm\sqrt{\frac{g}{d}}(2\eta_i - \eta) \tag{7}$$

including the surface elevation signal of the incident wave η_i. In addition, all the lateral walls are represented by closed boundaries with zero flux velocity (Stelling and Zijlema, 2003). To avoid wave reflection from the downwave end of the domain, a sponge layer (Dingemans, 1997) with a length of at least 3 times L was used in all geometries and additional lateral sponge layers were used in the 3D geometry (Fig. 4).

Finally, for the bottom friction a formulation based on Manning's roughness coefficient n was chosen to compute the bottom friction coefficient c_f as

$$c_f = \frac{n^2 g}{d^{1/3}} \tag{8}$$

In the present study, $n = 0.009$ s/m$^{1/3}$ for glass was chosen for all geometries to mimic the 2D experimental conditions in Heller and Spinneken (2015).

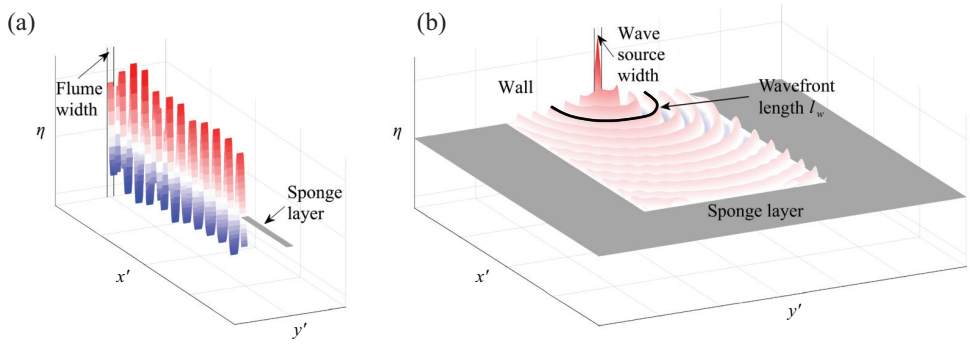

Figure 4: Three-dimensional schema of waves in (a) 2D and (b) 3D.

2.4. Calibration and validation

The calibration was performed to optimise the computational grids. The grids followed the Deltares (2018) guidelines with respect to orthogonality, smoothness, aspect ratio and minimum number of grid per wavelength. The orthogonality defines the difference of the angles between crossing grid lines from 90° where zero corresponds to orthogonal. This value was less than 0.04 everywhere in the computational domains. The smoothness parameter defines the variation in size of two adjacent cells and a value of $\leq$1.1 was used. Furthermore, the aspect ratio takes the difference in length between the opposing sides of a cell into account. Negligible differences in the rate of convergence of the solution were noted with maximum ratio in the order of 10 at the wave generation boundary as the values rapidly decrease with distance from the wave source. The number of grid points per wavelength was at least 45. This is a finer resolution than in van Vledder and Zijlema (2014) who used 25 grid points per wavelength resulting in good agreement with theory in SWASH for diffraction at a semi-infinite breakwater.

The 3D geometry with approximate linear waves was used to investigate the convergence for $\Delta x' = \Delta y' = 2.5, 5.0$ and 10.0 cm and the symmetry (Appendix A) of the solution. Approximate linear waves were used as they resulted in the smallest number of grid points per L among the wave types considered in this study. Fig. 5 shows the water surface at $r'/h = 3.0$ and 35.0 for all chosen grid resolutions indicating convergence for 5.0 cm. The final resolution was set to 2.5 cm to also satisfy the minimum value of grid points per L. SWASH matches higher order dispersion relations depending on the number of layers over the water depth. Higher values of kh, with k as the wave number, require a larger number of layers which shows indirectly the importance of wave dispersion for different kh values. 2 layers were chosen which results in a maximum error of 1% with $kh \leq 7.7$ (SWASH, 2016). Linear and Stokes waves were simulated using an higher order upwind discretisation scheme for the vertical advection term

of the $\overline{u}$-momentum equation, while the default 1st order upwind scheme was used for cnoidal and solitary waves. This was only necessary to reduce numerical dissipation, observed in the Stokes and linear wave propagation for the default scheme, particularly in 2D (SWASH, 2016).

A further validation was performed with the diffraction theory of Morse and Rubenstein (1938), by solving the application derived for water waves by Carr and Stelzriede (1952). This theory was chosen as it includes the variability of the solution with γ' and it applies to $b'/L \leq 0.5$, which is compatible with most landslide-tsunamis. The results in 3D for the approximate linear waves are compared to this theory for validation, as the diffraction theory is based on linear waves. The comparison is shown in Section 3.1.2 and the computation of the diffraction theory is explained in Appendix B.

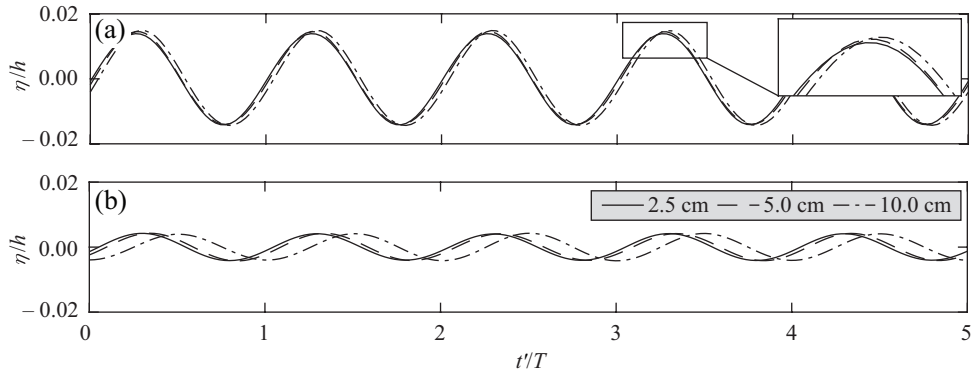

Figure 5: Wave profile convergence tests for approximate linear waves in the 3D geometry at (a) $r'/h = 3.0$ and (b) $r'/h = 35.0$.

3. Results

3.1. Idealised waves

3.1.1. Water surface time series

η for all idealised wave types was investigated in all geometries. Figs. 6, 7 and 8 show the relative water surface elevation η/h over $5T$ at 4 different r'/h. The profiles shown in Fig. 6 are obtained for approximate linear waves in deep water with $h/L = 0.50$ and a weak non-linearity $H/h = 0.067$. Fig. 6 shows how the water body geometry affects the waves. By comparing the wave profiles in 2D to the ones in the 7.5° geometry at $r'/h = 3.0$ (Fig. 6a) only a relatively small difference is observed. This ratio progressively increases also with the angle θ resulting in the smallest waves in 3D. The ratio of the wave heights between 2D and all other geometries also progressively increases with relative distance (Fig. 6b,c). At $r'/h = 35$ (Fig. 6d) the ratio between the waves in the 2D and 7.5° geometries is a factor of 3.2 and between 2D and 3D even a factor of 7.8.

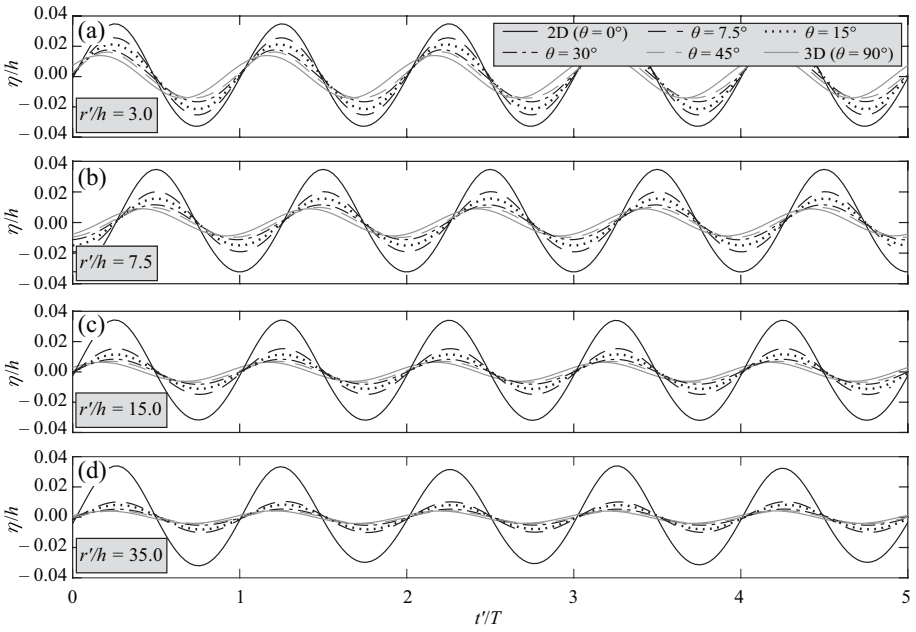

Figure 6: Relative water surface elevation η/h versus time normalised with the wave period t'/T for linear wave input in all geometries at different relative distances r'/h.

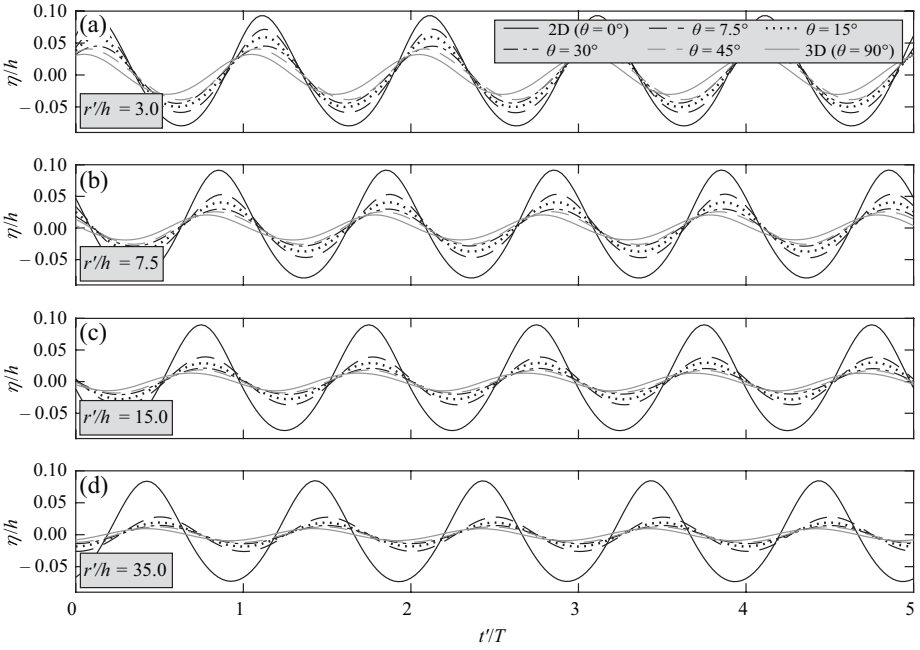

Figure 7: Relative water surface elevation η/h versus time normalised with the wave period t'/T for 5^{th} order Stokes waves in all geometries at different relative distances r'/h.

Water surface time series for Stokes waves characterised by a ratio $h/L = 0.39$ are shown in Fig. 7 at $r'/h = 3.0$, 7.5, 15.0 and 35.0. The Stokes wave heights in Fig. 7d show differences of a factor of 2.8 between the 2D and 7.5° geometry and 8.4 between 2D and 3D. The simulated cnoidal waves are shown in Fig. 8 with $h/L = 0.10$, which propagate in shallower water than Stokes waves. At $r'/h = 3.0$ (Fig. 8a) in the geometry $\theta = 15°$ a secondary peak in the wave troughs starts to develop which becomes larger with increasing θ. This is associated with frequency dispersion resulting in an additional shorter wave as shown in Fig. 8b-d with a different celerity relative to the primary wave. At $r'/h = 35$ all the dominant waves, except the one in 2D, show a decrease in celerity with decreasing wave height. In Fig. 8d the ratio between the wave heights between the 2D and $\theta = 7.5°$ geometry is 2.5 and between 2D and 3D it is 6.5, which is smaller than for Stokes waves (Fig. 7).

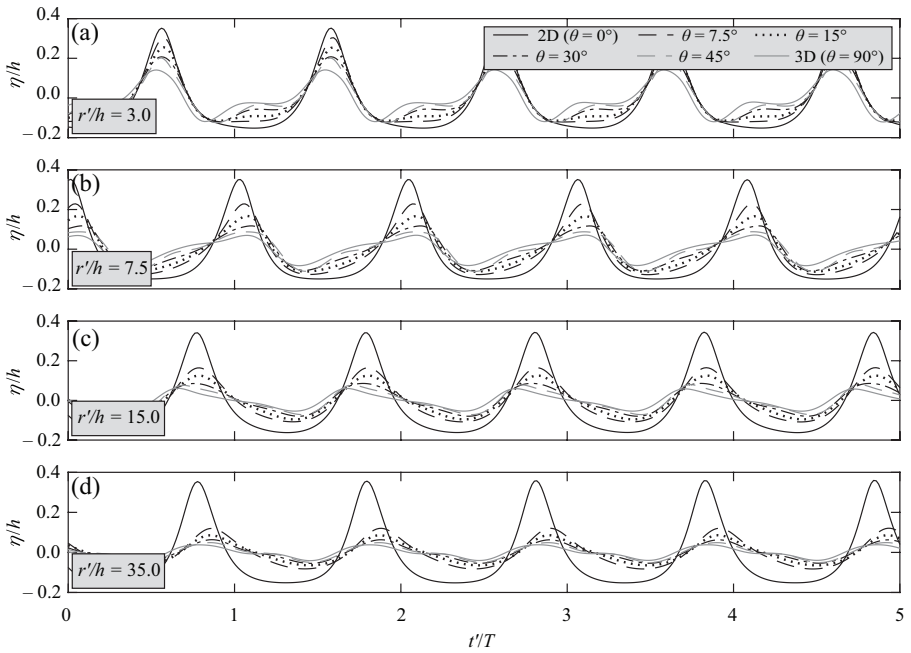

Figure 8: Relative water surface elevation η/h versus time normalised with the wave period t'/T for 5^{th} order cnoidal waves in all geometries at different relative distances r'/h.

The results for the solitary waves are shown in Fig. 9. The solitary wave profile is preserved at all relative distances in 2D. In all other geometries an increasing tail in both amplitude and length is formed at $r'/h = 3.0$. Further, the wave profile ratio between 2D and 3D at $r'/h = 35.0$ is a factor of 7.0 matching the results of Heller and Spinneken (2015). The ratio between a and a_t is clearly changing with r'/h affecting the main wave characteristics. For the wave in 3D the ratios a/a_t decrease from 2.3 at $r'/h = 3.0$ to 1.1 at $r'/h = 35.0$

(Fig. 9d). For the other geometries at $r'/h = 35.0$ the ratios a/a_t are 3.8 for 7.5°, 2.6 for 15°, 1.8 for 30° and 1.5 for 45°. For comparison, at $r'/h = 3.0$ the ratios are $a/a_t = 11.8$, 8.2, 6.0 and 4.5 for $\theta = 7.5°$, 15°, 30° and 45° respectively, with an almost constant difference of 3 times the values found at $r'/h = 35.0$. This shows that the waves approach the value $a/a_t = 1$, which is characteristic for linear waves, with both increasing θ and distance. This illustrates that the water body geometry not only affects the wave decay but also the wave non-linearity.

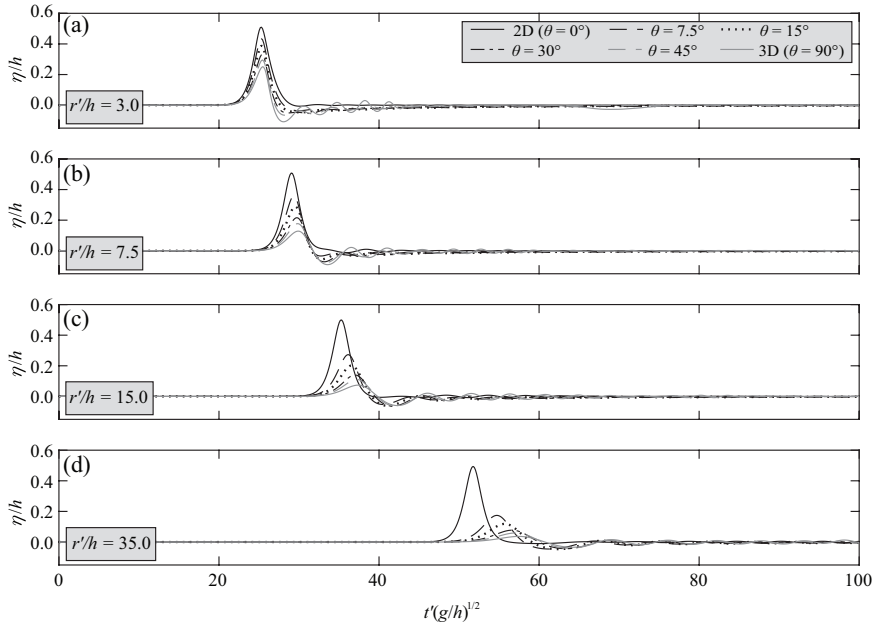

Figure 9: Relative water surface elevation for 1st order solitary waves in all geometries at different relative distances r'/h.

3.1.2. Wave height decay

The wave height H was calculated as the average over $5T$ (apart from the solitary wave). Values were calculated for all wave types and geometries at the locations shown in Table 1. Fig. 10 shows H/h for cnoidal waves over the relative distance for each geometry for $\gamma' = 0°$. This clearly confirms the increasing decay of H with θ as highlighted in Section 3.1.1. The wavefront length l_w was identified as an excellent parameter to link the wave decay of the idealised waves across all water body geometries. The waves propagate with semi-circular fronts from the source. For a linear wave $Ec_g l_w =$ constant, E being the mean energy density per unit area and c_g being the group velocity. Given that h is constant in all simulations the previous relationship reduces to $El_w =$ constant. In addition, if the source width b' is relatively small, it can also be approximated as a line.

The values of l_w are then calculated for the numerical results as

$$l_w(r', \theta) = b' + 2r'\theta_{rad} \tag{9}$$

with the radial distance r' and the water body side angle θ_{rad} in radians. The resulting values based on Eq. (9) are shown in Table C.1 for each wave type. This parameter l_w normalised with the water depth h (i.e. l_w/h) is used to correlate H/h for all idealised wave types in Fig. 11.

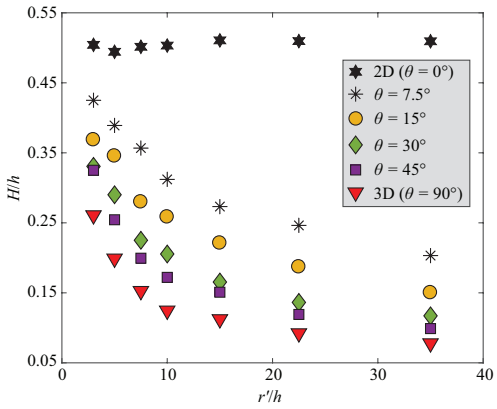

Figure 10: Relative wave height H/h decay with relative radial distance r'/h for the 5^{th} order cnoidal waves in all geometries.

Fig. 11 shows H/h versus l_w/h for all wave types with the wave heights in different geometries highlighted with different markers. The diffraction theory from Carr and Stelzriede (1952) using Eq. (B.2) is plotted as a dashed black line. Furthermore, Green's law was included as

$$H(r', \theta) = H(r' = 0, \theta = 0°) \left(\frac{b'}{l_w(r', \theta)} \right)^{1/2} \left(\frac{h(r' = 0)}{h(r')} \right)^{1/4}, \tag{10}$$

where $H(r', \theta)$ is the wave height in function of r', $l_w(r', \theta)$ and $h(r')$ are the associated wavefront length and water depth, respectively. $H(r' = 0, \theta = 0°)$ is the wave height at the source in 2D and b' is the source width. In the idealised geometries $h(r')$ is constant, such that the last term on the right-hand side of Eq. (10) reduces to 1. This equation can easily be applied by known wave characteristics at the source in 2D. The results for each wave type are then tested with the normalised Root Mean Square Error

$$nRMSE = \frac{\sqrt{\frac{1}{\mathrm{N}} \sum_{\mathrm{i}}^{\mathrm{N}} \left(y_{pred,\mathrm{i}} - y_{num,\mathrm{i}} \right)^2}}{\left(y_{num,max} - y_{num,min} \right)} \tag{11}$$

where $y_{pred,\mathrm{i}}$ is the i-th sample of the predicted parameter and $y_{num,\mathrm{i}}$ is the corresponding numerical value. N is the number of considered samples, $y_{num,max}$

and $y_{num,min}$ are respectively the maximum and the minimum numerical values in the range considered ($nRMSE = 0$ represents perfect agreement). A similar equation to Eq. (10) can be obtained for the linear wave amplitude (Green, 1838) by replacing H with the positive wave amplitude a in Eq. (10) resulting in

$$a(r', \theta) = a(r' = 0, \theta = 0°) \left(\frac{b'}{l_w(r', \theta)} \right)^{1/2} \left(\frac{h(r' = 0)}{h(r')} \right)^{1/4}. \tag{12}$$

Note that Eq. (12) will be applied to non-linear waves as a simplification hereafter. Fig. 11a shows that all H/h for approximate linear waves in all geometries, apart from 3D, collapse on one curve corresponding to Green's law. Diffraction theory (Appendix B) under-predicts the wave height decay in the intermediate geometries but perfectly agrees with the wave heights observed in 3D, given that this theory is based on linear waves for very similar 3D conditions (Section 1.2).

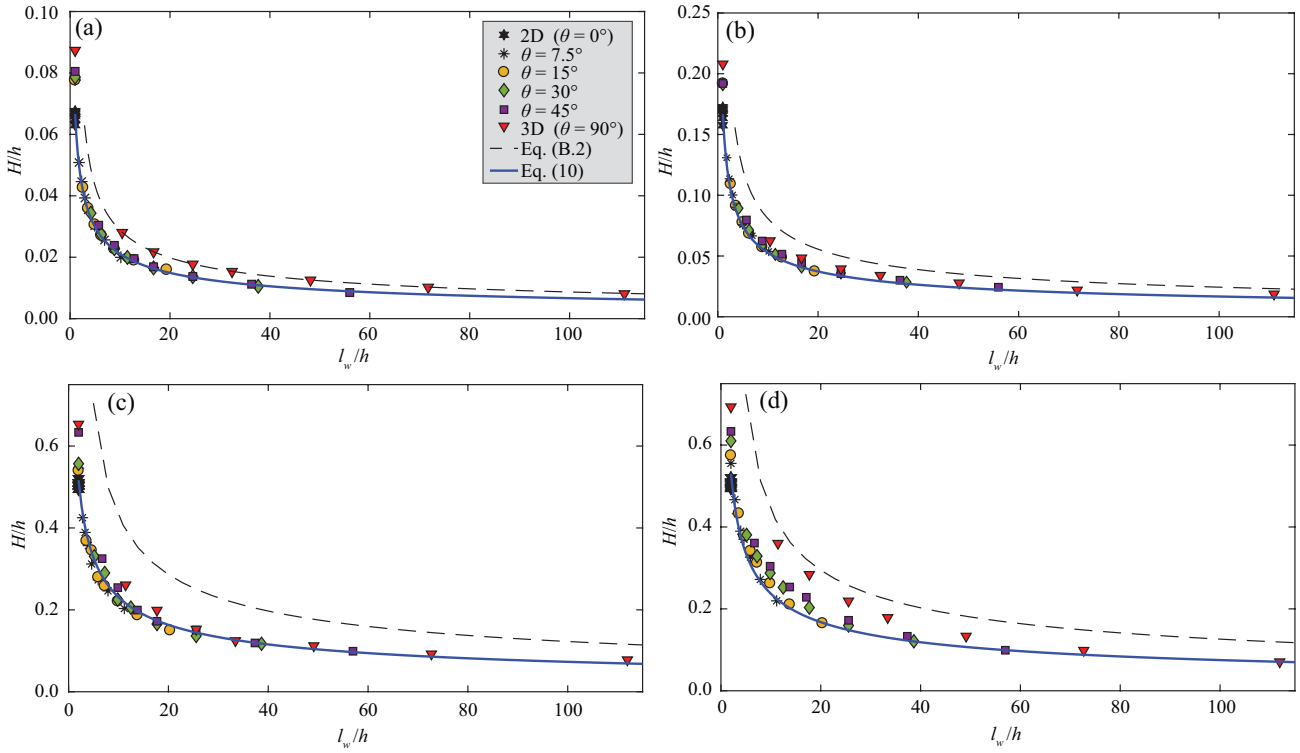

Figure 11: Relative wave height H/h decay with l_w/h for (a) approximate linear waves, (b) 5^{th} order Stokes waves, (c) 5^{th} order cnoidal waves and (d) 1^{st} order solitary waves in all investigated geometries compared to Green's law (Eq. (10)) ((a) $nRMSE = 0.06$, (b) $nRMSE = 0.06$, (c) $nRMSE = 0.05$, (d) $nRMSE = 0.08$) and diffraction theory (Eq. (B.2)).

For Stokes waves shown in Fig. 11b, the diffraction theory under-predicts the wave height decay in all geometries, which is not surprising given that the considered theory is based on linear wave theory. Fig. 11c shows a similar decay curve for cnoidal waves. In this case the data move further away from diffraction theory. For example, at $l_w/h = 20$ the ratio between the numerical values and the values calculated by diffraction theory (Carr and Stelzriede, 1952) is 0.56 (Fig. 11c). This difference appears to be very sensitive to the ratio b'/L used to calculate Eq. (B.2); larger ratios (Fig. 11a, b) result in a closer agreement with the simulated results than smaller ratios (Figs. 11c).

Fig. 11d shows the wave decay for solitary waves. The data scatter relative to Green's law in the range $6 < l_w/h < 40$ is larger than for the other wave types. For $l_w/h < 6$ and $l_w/h > 40$ there is still a close match between the data and Eq. (10). The largest difference from Green's law is found for the 3D geometry with up to 40% difference in wave height. Fig. C.1 shows the corresponding results for the wave amplitudes, as for the wave heights shown in Fig. 11, compared with Eq. (12) (Appendix C).

3.1.3. Lateral wave energy spread

In this section the lateral wave energy spread for each wave type is investigated. The wave height is investigated with a resolution of $\Delta\gamma' = 7.5°$ at different r'/h.

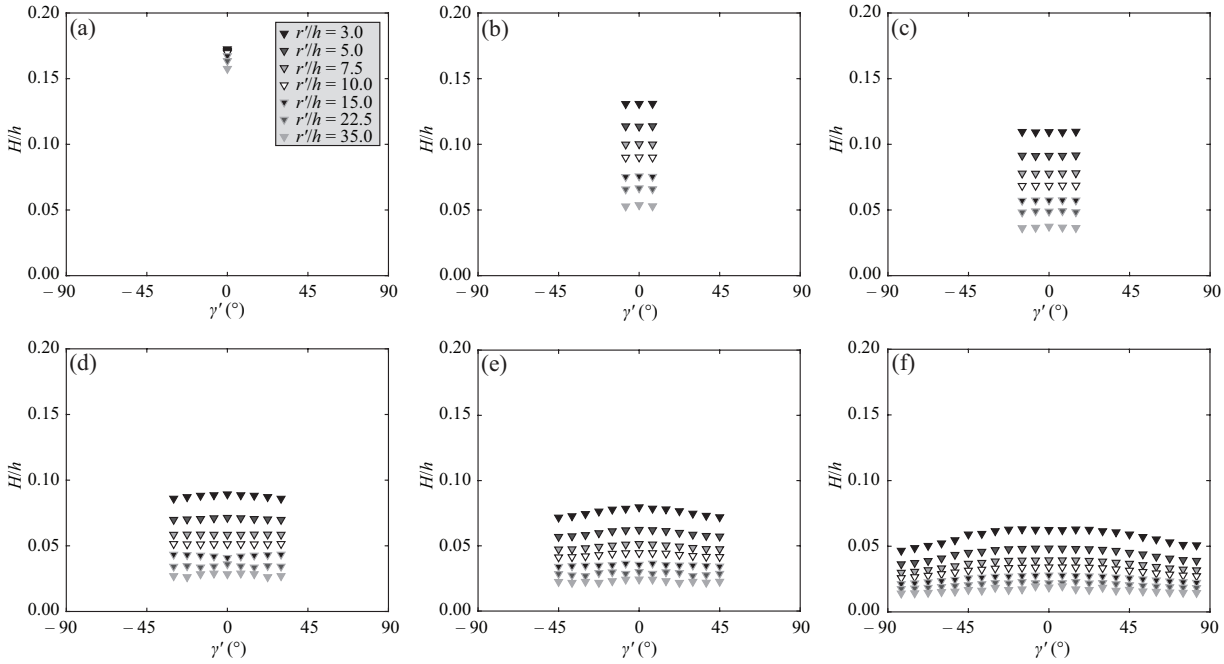

Figure 12: Relative wave heights H/h for Stokes waves as a function of the propagation angle γ' and the relative radial distance r'/h for (a) 2D ($\theta = 0°$), (b) $\theta = 7.5°$, (c) $\theta = 15°$, (d) $\theta = 30°$, (e) $\theta = 45°$ and (f) 3D ($\theta = 90°$).

Fig. 12 shows the spatial distribution of the wave heights for the 5$^{\text{th}}$ order Stokes waves (the other wave types are shown in Appendix D) with different r'/h values represented by different grey shades. The lateral wave decay becomes important with increasing θ. Fig. 12f shows that the maximum wave heights at $\gamma' = 0°$ are $20 - 34\%$ larger than at $\gamma' = \pm 82.5°$.

Green's law is used to correlate the lateral decay of H with the propagation angle γ' in all investigated geometries. Fig. 13 shows H normalised by using Eq. (10), on the y-axis, over the wave propagation angle γ' for all simulated wave types. Green's law is represented by a blue circle.

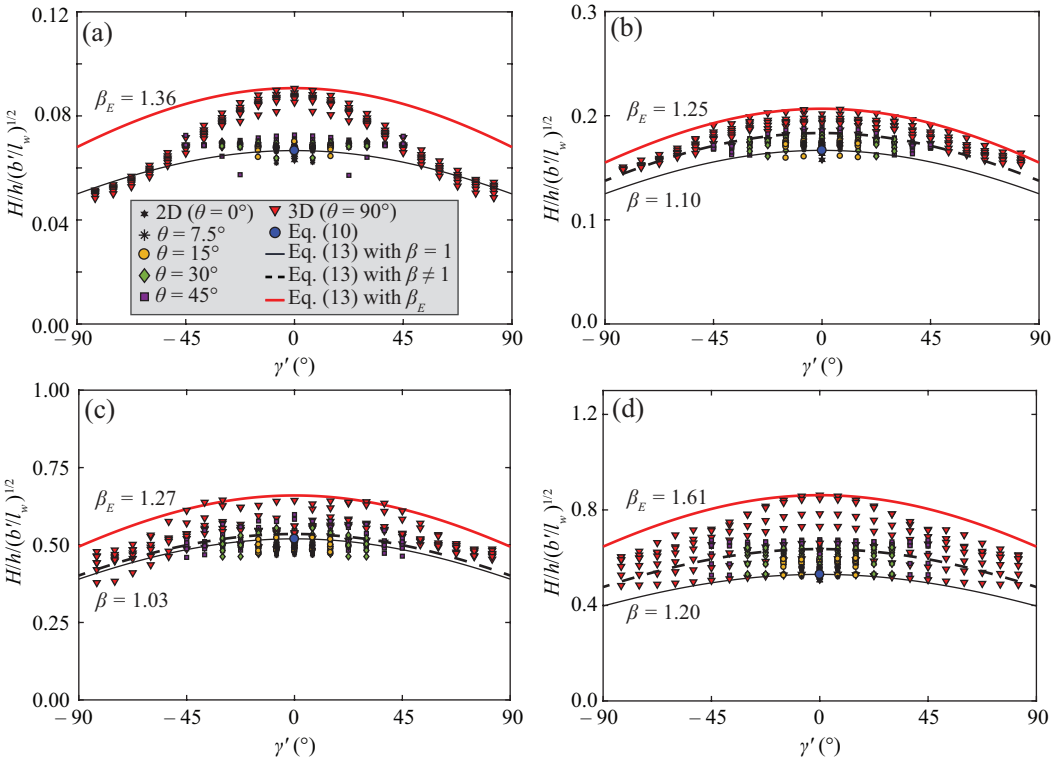

Figure 13: Lateral wave decay for (a) approximate linear waves, (b) 5$^{\text{th}}$ order Stokes waves, (c) 5$^{\text{th}}$ order cnoidal waves and (d) 1$^{\text{st}}$ order solitary waves for all investigated geometries, compared to Eq. (13).

The decay term $\cos^2(\gamma'/3)$ is inspired by Heller and Spinneken (2015) and Huber and Hager (1997) where $\cos^{2\{1+\exp[-0.2(r/h)]\}}(2\gamma/3)$ and $\cos^2(2\gamma/3)$, respectively, have been found for experimental data based on the 3D geometry. The value 2/3 is reduced to 1/3 herein to better represent the data. This smaller lateral wave decay is associated with the lack of slide momentum in the far field, where the present results apply, in contrast to Heller and Spinneken (2015) and Huber and Hager (1997) involving also the near field with a larger lateral decay. To reproduce the lateral decay trend in the far field, the empirical term

$\cos^2(\gamma'/3)$ is added to the theoretical Eqs. (10) and (12) resulting in

$$\frac{H(r',\gamma',\theta)}{h} \Big/ \left(\frac{b'}{l_w(r',\theta)}\right)^{1/2} = \beta \frac{H(r'=0,\gamma'=0°,\theta=0°)}{h} \cos^2\left(\frac{\gamma'}{3}\right) \quad (13)$$

$$\frac{a(r',\gamma',\theta)}{h} \Big/ \left(\frac{b'}{l_w(r',\theta)}\right)^{1/2} = \beta \frac{a(r'=0,\gamma'=0°,\theta=0°)}{h} \cos^2\left(\frac{\gamma'}{3}\right) \quad (14)$$

where $H(r',\gamma',\theta)$ and $a(r',\gamma',\theta)$ are the wave height and amplitude at the position r' and γ', $l_w(r',\theta)$ the corresponding wavefront length (Table C.1) and $H(r'=0,\gamma'=0°,\theta=0°)$ and $a(r'=0,\gamma'=0°,\theta=0°)$ are the 2D wave height and amplitude, respectively. The water depth h = constant is maintained in Eqs. (13) and (14) to keep the equations in dimensionless form. An empirical pre-factor can be applied to $H(r'=0,\gamma'=0°,\theta=0°)$ and $a(r'=0,\gamma'=0°,\theta=0°)$ to determine the upper envelope (β_E) and the best overall fit (β) of the numerical data. β is based on the smallest $nRMSE$, which together with the corresponding $\pm$% scatter are summarised in Table 3 for both H and a.

Table 3: Pre-factors for wave height H (Eq. (13)) and wave amplitude a (Eq. (14)) for each investigated wave type. The upper envelope is determined with β_E and the best overall fit to the data in Fig. 13 with β.

	H			a		
Wave theory	β_E	β ($nRMSE$)	$\pm$ scatter	β_E	β ($nRMSE$)	$\pm$ scatter
Approximate linear	1.36	-	-	1.36	-	-
5^{th} order Stokes	1.25	1.10 (0.17)	+13%, −14%	1.18	1.01 (0.14)	+17%, −14%
5^{th} order cnoidal	1.27	1.03 (0.16)	+23%, −12%	1.09	0.85 (0.21)	+26%, −39%
1^{st} order solitary	1.61	1.20 (0.21)	+36%, −21%	1.14	0.84 (0.23)	+36%, −38%

The black curve in Fig. 13 represents Eq. (13) with $\beta = 1$, the red line with β_E and the dashed line with β. For the approximate linear waves, only the line with β_E is presented as the main purpose to include this wave type herein is to link the numerical results to theory rather than to predict landslide-tsunamis, given that they are generally not linear. Stokes waves result in the smallest $\beta_E = 1.25$ for H requiring only 25% increase from the semi-theoretical expression to reach the upper envelope. The best fit is achieved with $\beta = 1.10$ with a data scatter of +13% and −14%. For cnoidal waves (Fig. 13c) $\beta_E = 1.27$ and $\beta = 1.03$ with a data scatter of +23% and −12%. Finally, the solitary waves (Fig. 13d) result in the largest difference between the black and the red curves with $\beta_E = 1.61$ and $\beta = 1.20$ with a data scatter of +36% and −21%. For the solitary wave the black curve corresponds simultaneously to a lower envelope of the values. This is already indicated in Fig. 11d where all points lay above Green's law. The corresponding values for the wave amplitude a for each wave type are also shown in Table 3. In this case the best fit is always achieved for $\beta < 1$, except for Stokes waves, while $\beta_E > 1$. Fig. C.2 shows the corresponding data.

Fig. 13b-d allow for a semi-theoretical prediction of idealised tsunami heights for all investigated wave types, geometries and locations. These predictions take the effect of the water body geometry into account as well as bottom friction. However, they are based on idealised wave types, which propagate as wave trains of constant H, unlike real tsunamis. This creates differences in wave propagation which are investigated in Section 3.2 based on experimental wave profiles.

3.2. Laboratory waves

Simulations of waves measured in the laboratory experiments of Heller and Hager (2011) were carried out to quantify to which extent frequency dispersion affects wave decay in 2D. The 2D geometry was chosen as it excludes the lateral energy spread and the wave decay may fully be attributed to frequency dispersion, if bottom friction is neglected. Experimental measurements (Heller and Hager, 2011) are compared with SWASH simulations based on both idealised time series essentially excluding frequency dispersion (Section 1.2) and real time series based on the same study.

3.2.1. Coupling criterion

To perform this comparison between idealised and laboratory waves, a criterion for the coupling location corresponding to the boundary between the wave generation and propagation zones (Fig. 2) is required. The impact radius r_i from Evers et al. (2019) and the location of the maximum wave amplitude x_M from Heller and Hager (2010) are considered. These criteria are given as:

$$r_i(\gamma = 0°) = 2.5[\mathrm{P}B\cos(6/7\alpha)]^{1/4}h \tag{15}$$

$$x_M = (11/2)\mathrm{P}^{1/2}h. \tag{16}$$

$\mathrm{P} = \mathrm{F}S^{1/2}M^{1/4}[\cos(6/7\alpha)]^{1/2}$ is the impulse product parameter (Heller and Hager, 2010), $B = b/h$ the relative slide width and α the slide impact angle. P includes the slide Froude number $\mathrm{F} = V_s/(gh)^{1/2}$ with the slide centroid velocity V_s at impact, the relative slide thickness $S = s/h$ with the slide thickness s at impact and the relative slide mass $M = m_s/(\rho_w b h^2)$ with the slide mass m_s and the water density ρ_w. The coupling locations based on Eqs. (15) and (16) move further downstream for more violent slide impacts and wave generation. Both r_i and x_M depend solely on the landslide parameters, which are anyway required for landslide-tsunami hazard assessment. The slide parameters and the potential coupling locations, computed with Eqs. (15) and (16) for each investigated wave type, are summarised in Table 4.

To work on the safe side, the coupling location is selected at the wave gauge located downwave of both r_i/h and x_M/h. The first wave gauge position of Heller and Hager (2011) that satisfies $d_M/h = x/h \geq \max(r_i/h; x_M/h)$ is also included in Table 4. This position was chosen as coupling location and wave generation for both simulations based on the laboratory time series and idealised waves.

Table 4: Slide parameters and coupling locations based on Eqs. (15) and (16) for each wave type.

Wave type	B	S	M	F	α	P	Eq. (15)	Eq. (16)	coupling location
Stokes-like	0.50	0.23	0.11	1.36	45°	0.33	1.50	3.16	$x/h = 4.55$
Cnoidal-like	0.50	0.40	0.45	2.27	45°	1.03	1.99	5.58	$x/h = 8.10$
Solitary-like	0.50	0.81	0.90	3.77	90°	1.55	1.61	6.85	$x/h = 8.57$

3.2.2. Effects of frequency dispersion

Figure 14 shows the wave profiles at 3 different positions for a Stokes-like landslide-tsunami. The decay of the idealised waves is negligible whereas both the laboratory and the real time series show a similar decay. This shows that the primary wave decay for Stokes-like waves in 2D is mainly caused by frequency dispersion as indicated by the increase of the tail waves in Fig. 14a to c. Frequency dispersion is negligible for idealised waves where the wave profiles remain stable. To quantify frequency dispersion the ratios a_l/a_c and H_l/H_c are calculated, with a_l and H_l as the wave amplitude and height at the last wave gauge position (Figs. 14c, 15c, 16c) in Heller and Hager (2011) and a_c and H_c as the wave amplitude and height at the coupling location. These ratios are given in Table 5.

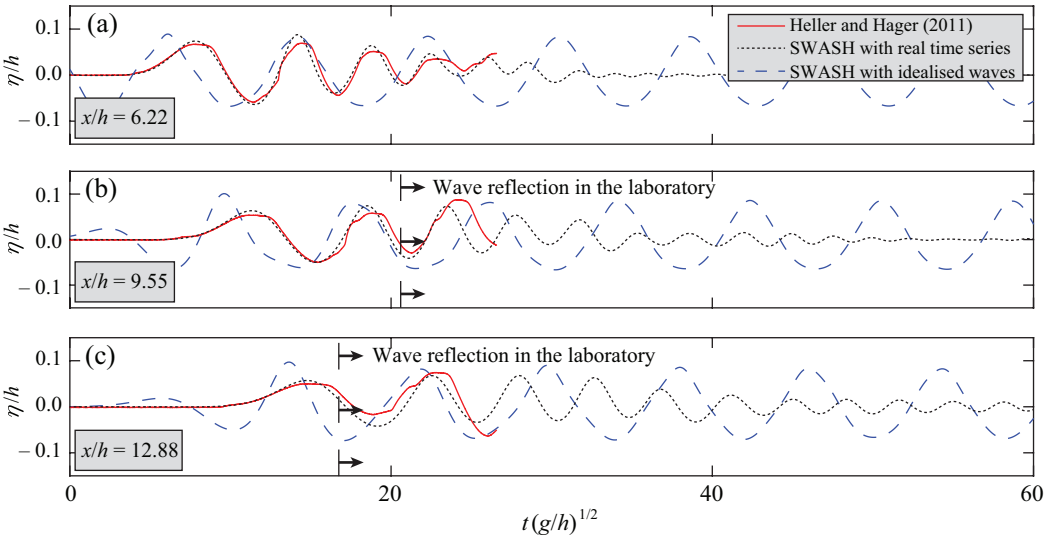

Figure 14: Comparison of 2D laboratory measurements of Stokes-like waves, real time series and 5$^{\text{th}}$ order idealised Stokes wave SWASH simulations: relative water surface elevation η/h at different relative distances x/h.

Similar values of $a_l/a_c = 0.66$ and 0.73 are found for the laboratory measurements and real time series simulations, respectively, confirming the capability of SWASH to simulate frequency dispersion reasonably well for Stokes-like

waves. However, for the idealised Stokes waves a value of $a_l/a_c = 0.96$ and even $H_l/a_c = 0.99$ is found confirming the small wave decay due to bottom friction.

The cnoidal-like and solitary-like waves are shown in Figs. 15 and 16. Cnoidal-like waves decay much slower than Stokes-like waves (Fig. 14) when considering that the investigated maximum relative distance for cnoidal-like waves is twice as large. Very similar a_l/a_c laboratory measurement and numerical ratios for the cnoidal-like wave profiles are found namely 0.79-0.86 (Table 5).

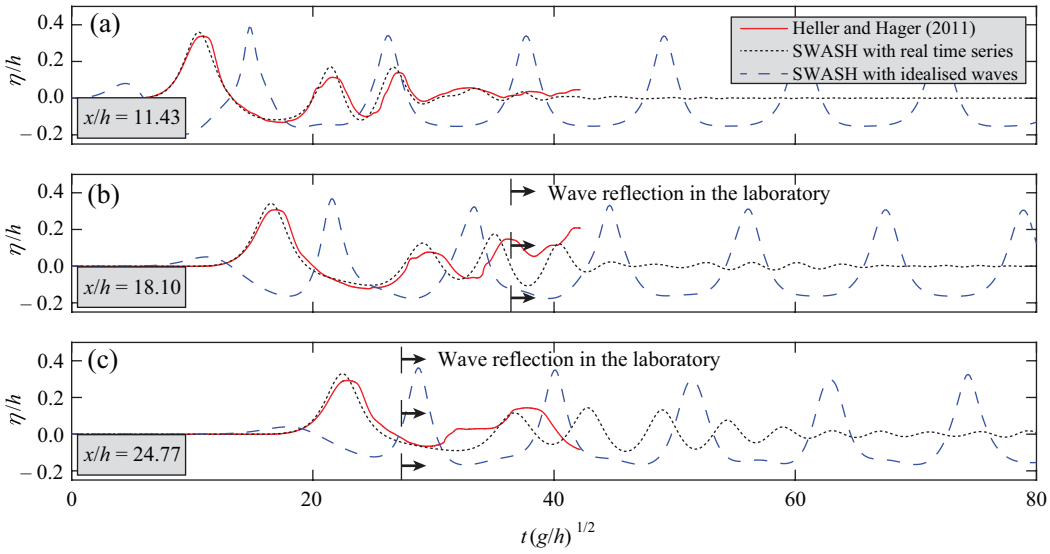

Figure 15: Comparison of 2D laboratory measurements of cnoidal-like waves, real time series and 5^{th} order idealised cnoidal SWASH wave simulations: relative water surface elevation η/h at different relative distances x/h.

However, when considering H_l/H_c it becomes clear that cnoidal-like waves are also affected by frequency dispersion. In fact, there is a difference of 12% between the simulations with the experimental time series ($H_l/H_c = 0.78$) and idealised waves ($H_l/H_c = 0.90$). The results for solitary-like waves (Fig. 16) show an even closer match between laboratory measurements, real time series and idealised waves than cnoidal-like waves. Equal $a_l/a_c = H_l/H_c = 0.90$ for real and idealised wave simulations are observed and only a 8% difference to the laboratory measurements is found.

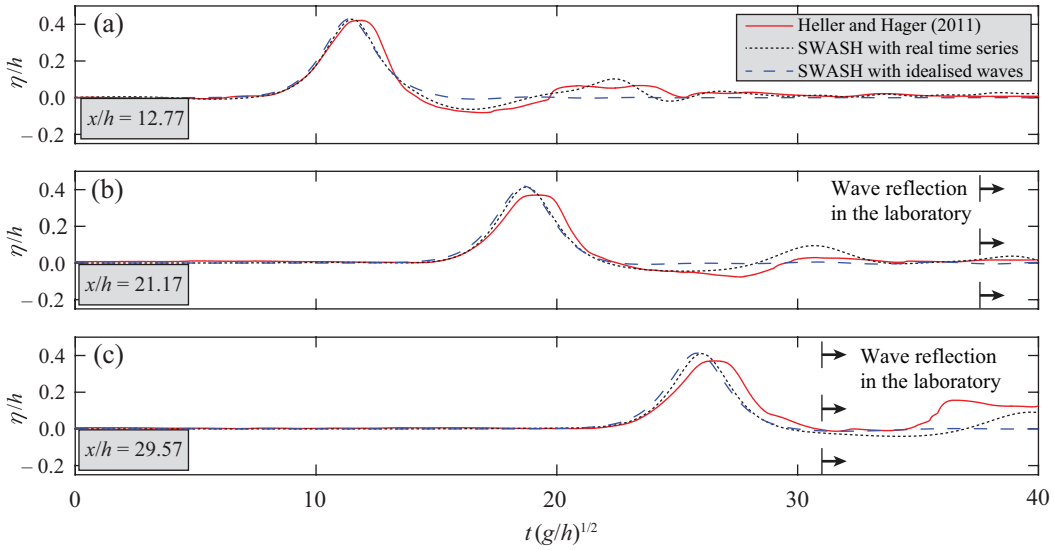

Figure 16: Comparison of 2D laboratory measurements of solitary-like waves, real time series and 1st order idealised solitary SWASH wave simulations: relative water surface elevation η/h at different relative distances x/h.

Table 5: Wave decay ratios between wave amplitude a_l and height H_l at the last wave gauge position in Heller and Hager (2011) and the wave amplitude a_l and height H_c at the coupling location for each wave type (* measurements affected by reflection).

Wave type	Gauge at coupling location	Location of last gauge	Heller and Hager (2011)	SWASH real time series	SWASH idealised waves
			a_l/a_c ($[(a_l/a_c)-1\,]\times100$)		
Stokes(-like)	$x/h = 4.55$	$x/h = 12.88$	0.66 (-34%)	0.73 (-27%)	0.96 (-4%)
Cnoidal(-like)	$x/h = 8.10$	$x/h = 24.77$	0.79 (-21%)	0.86 (-24%)	0.83 (-17%)
Solitary(-like)	$x/h = 8.57$	$x/h = 29.57$	0.83 (-17%)	0.90 (-10%)	0.90 (-10%)
			H_l/H_c ($[(H_l/H_c)-1\,]\times100$)		
Stokes(-like)	$x/h = 4.55$	$x/h = 12.88$	0.51 (-49%)*	0.80 (-20%)	0.99 (-1%)
Cnoidal(-like)	$x/h = 8.10$	$x/h = 24.77$	0.69 (-31%)*	0.78 (-22%)	0.90 (-10%)
Solitary(-like)	$x/h = 8.57$	$x/h = 29.57$	0.83 (-17%)	0.90 (-10%)	0.90 (-10%)

These results show that the contribution of frequency dispersion on wave decay changes with the wave type. The mismatch of H_l/H_c for the laboratory Stokes-like and cnoidal-like tsunamis is due to wave reflection (Fig. 14c, Fig. 15c) affecting the primary wave trough (Table 5). This confirms that the effect of frequency dispersion on wave decay in 2D decreases with increasing non-linearity of the wave type. This further shows that the findings based on the idealised waves (Section 3.1) apply well to landslide-tsunamis in proximity of the shallow-water wave regime (solitary-like waves), but may overestimate landslide-tsunamis closer to the deep-water regime (Stokes-like waves) where frequency dispersion accounts for up to $34\% - 4\% = 30\%$ of the wave decay.

4. Discussion

In this section the new findings are discussed in relation to already available knowledge. The idealised waves essentially address the effect of the lateral energy spread and neglect frequency dispersion. Laboratory measurements are compared to the idealised waves propagating in the far field to quantify whether the effect of the lateral energy spread or frequency dispersion is more dominant. Further, Eqs. (13) and (14) are applied to the 2014 Lake Askja landslide-tsunami to illustrate the application of the new semi-theoretical equations.

4.1. Relevance of the water body geometry for idealised waves

The ratio b'/L and the wave non-linearity H/h were found to be very important for the effect of the water body geometry as they significantly affect the wave decay inside a water body and determine how closely the diffraction theory of Carr and Stelzriede (1952) matches the numerical data. This can clearly be seen by comparing the results in Figs. 11b and Fig. 11c where the Stokes waves result in a closer match to diffraction theory than cnoidal waves. The two parameters b'/L and H/h, however, do not seem to affect the match with Green's law (Eq. (10)) that follows all numerical data closely except for solitary waves in Fig. 11d where the 3D geometry shows a noticeable difference, in the range $6 < l_w/h < 40$.

The water body geometry has also an effect on the observed wave type. In fact, the solitary wave transforms in a Stokes wave in 3D as indicated by $a/a_t = 1.07$ in Fig. 9d. This agrees with Heller and Spinneken (2015) where the more energetic solitary and bore-like waves were only observed in 2D and only Stokes-like and cnoidal-like waves were observed in 3D by identical slide scenarios.

The effect of the water body geometry for idealised waves was correlated with l_w used in the Green's law (Eqs. (10) and (12)). This allows for a much broader application of the findings of Chang et al. (1979) for solitary waves where the width of the diverging channel rather than l_w was used. Further, the semi-theoretical Eqs. (13) and (14) were derived to predict the lateral wave decay. Using these equations, with a different pre-factor β_E for the upper envelope and β for the best fit of the data for each wave type, allows for the calculation of the maximum wave heights and amplitudes in all investigated geometries, for all propagation angles and distances for idealised waves (excluding frequency dispersion). Given that for all herein investigated scenarios the idealised waves produced larger waves than the real waves (including frequency dispersion) in 2D (Table 5), the semi-theoretical equations in Section 3.1.3 tend to over-predict real landslide-tsunamis and tend to work on the safe side.

4.2. Relevance of lateral energy spread and frequency dispersion

Table 6 shows the ratios a_l/a_c and H_l/H_c of the idealised waves. This helps to separate the contributions of the lateral energy spread and frequency dispersion on wave decay as the idealised waves essentially consider the former effect only.

Table 6 also includes the values of Table 5 of the idealised waves in 2D for comparison. All values in Table 6 are lower than the values calculated in Table 5 indicating that the lateral energy spread is more important than frequency dispersion, already for $\theta = 7.5°$. The differences between the values in Table 5 and 6 further increase with θ. For example, Table 5, shows $a_l/a_c = 0.66$, 0.79 and 0.83 for Stokes-like, cnoidal-like and solitary-like tsunamis in 2D and the corresponding values for $\theta = 7.5°$ in Table 6 are 0.46, 0.43 and 0.45. This also shows that the solitary wave is the most affected wave type by the effect of the lateral energy spread with $a_l/a_c = 0.14$ for 3D (Table 6) against 0.83 for laboratory measurements in 2D (Table 5).

Table 6: Idealised wave decay ratios between wave amplitude a_l and height H_l at the last experimental wave gauge position used in Section 3.2 (Heller and Hager, 2011) and the wave amplitude a_c and height H_c at the numerical wave source (coupling location).

Wave type	Location of last gauge (x'/h or r'/h)	2D ($\theta = 0°$)	$\theta = 7.5°$	$\theta = 15°$	$\theta = 30°$	$\theta = 45°$	3D ($\theta = 90°$)
				a_l/a_c ($[(a_l/a_c)-1\,]\times100$)			
Stokes	8.33	0.96 (−4%)	0.46 (−54%)	0.39 (−61%)	0.27 (−73%)	0.23 (−77%)	0.18 (−82%)
Cnoidal	16.70	0.83 (−17%)	0.43 (−57%)	0.31 (−69%)	0.25 (−75%)	0.23 (−77%)	0.16 (−84%)
Solitary	21.00	0.90 (−10%)	0.45 (−55%)	0.33 (−66%)	0.24 (−76%)	0.20 (−80%)	0.14 (−86%)
				H_l/H_c ($[(H_l/H_c)-1\,]\times100$)			
Stokes	8.33	0.99 (−1%)	0.50 (−50%)	0.36 (−64%)	0.29 (−71%)	0.25 (−75%)	0.16 (−84%)
Cnoidal	16.70	0.90 (−10%)	0.59 (−51%)	0.37 (−63%)	0.29 (−71%)	0.26 (−74%)	0.17 (−83%)
Solitary	21.00	0.90 (−10%)	0.50 (−50%)	0.38 (−62%)	0.27 (−73%)	0.21 (−79%)	0.15 (−85%)

4.3. Computation example

A procedure to predict landslide-tsunamis using Eqs. (13) and (14) is presented here. The present study only addresses wave propagation, while already available relationships for the 2D case (Heller and Hager, 2010) allow to compute the maximum wave height and its position in the wave generation zone. Note that the slide width b' at the coupling location is approximated with the slide width b from the impact zone plus an arc section on either side of the slide (Fig. 17). This approximation is necessary as a straight line at the coupling location (as in Fig. 3) would converge to infinity with increasing θ. This approximation also satisfies the energy flux conservation between $l_w(r' = 0, \theta)$ and $l_w(r', \theta)$, which coincides with the assumptions made for Green's law (Dean and Dalrymple, 1991).

The application procedure of Eq. (13) can be summarised with the following steps:

1. Define the landslide width b, thickness s, mass m_s, impact velocity V_s, slope angle α, density ρ_s, water density ρ_w and water depth h
2. Evaluate the wave type in 2D using the wave type product T of Heller and Hager (2011)
3. Calculate the maximum wave height H_M for 2D and its position from the slide impact $r = d_M$

4. Define θ_1 and θ_2 (Fig. 17) at the slide sides to approximate the current geometry to an idealised one up to $r' = 0$ and calculate the wave front length $l_w(r' = 0, \theta)$
5. Compute $H(r' = 0, \gamma' = 0°, \theta)$ by applying energy conservation

$$H(r' = 0, \gamma' = 0°, \theta) = H_M(r' = 0, \gamma' = 0°, \theta = 0°)[b/l_w(r' = 0, \theta)]^{1/2} \tag{17}$$

6. Define θ_3 and θ_4 (Fig. 17) at the slide sides to approximate the geometry up to a desired distance $r' > 0$, thereby taking any restrictions or expansions of the water body into account, and calculate $l_w(r', \theta)$
7. Use Eq. (13) to calculate $H(r', \gamma', \theta)$ at the desired location.

These steps are illustrated with the 2014 landslide-tsunami event in Lake Askja in Iceland.

The wave heights are computed at two different positions and compared with the numerical results of Gylfadóttir et al. (2017). The slide parameters are defined first (step 1). The slope angle is calculated by using the 500 m distance between the base of the rotational failure and the mean water level and the elevation difference between the same two points (92 m) resulting in $\alpha = \text{atan}(92/500) = 10.4°$. The effective friction coefficient is defined as $\mu = \Delta H/\Delta L$ where $\Delta H = 230$ m is the height difference of the slide centroid's initial and final positions and $\Delta L = 2450$ m is the horizontal distance between the same two points. This results in $\mu = 0.09$. This small friction coefficient indicates a hypermobile slide as observed in nature for large slide volumes exceeding 10^6 m^3 (Pudasaini and Miller, 2013), which is in line with the slide volume of 10×10^6 m^3 (considering a 30% porosity) in the Lake Askja case. The corresponding impact velocity is $V_s = \sqrt{2g(\sin\alpha - \mu\cos\alpha)\Delta x} = 30.1$ m/s (Körner, 1976) with $\Delta x = 500$ m as the distance from the initial position of the slide centroid to the SWL. This velocity is only 2.6% smaller than 30.9 m/s used by Gylfadóttir et al. (2017) as best fit for their simulations. The remaining slide parameters are summarised in Table 7 with the slide mass m_s computed based on the slide volume and a slide density of $\rho_s = 2000$ kg/m^3.

Table 7: Dimensional landslide parameters for the 2014 Lake Askja landslide-tsunami

b (m)	s (m)	α (°)	V_s (m/s)	m_s (kg)	ρ_s (kg/m^3)	ρ_w (kg/m^3)	h (m)
550.0	35.5	10.4	30.1	2×10^{10}	2000	1000	138.0

The wave type product $\text{T} = S^{1/3}M\cos[(6/7)\alpha] = 0.26^{1/3}1.91\cos[(6/7)10.4°] = 1.21$ (Table 8) is calculated to evaluate the wave type (step 2). The wave type product T for granular landslides is in the range of $4/5\text{F}^{-7/5} \leq \text{T} \leq 11\text{F}^{-5/2}$ ($1.06 \leq 1.21 \leq 18.06$) for which cnoidal and solitary-like waves are expected in 2D (Heller and Hager, 2011). The former wave type was chosen because T is closer to the lower boundary of the range where less energetic waves are expected hence $\beta = 1.03$ and $\beta_E = 1.27$ are selected.

The maximum wave height H_M is computed with $H_M = 5/9\text{P}^{4/5}h =$

Table 8: Non-dimensional landslide parameters for the Lake Askja landslide-tsunami

S	M	F	T	P	d_M (m)	H_M (m)	a_M (m)
0.26	1.91	0.82	1.21	0.49	531	43.3	34.7

$5/9 \cdot 0.49^{4/5}138 = 43.3$ m (Table 8) (Heller and Hager, 2010) for 2D with $\mathrm{P} = \mathrm{F}S^{1/2}M^{1/4}\{\cos[(6/7)\alpha]\}^{1/2} = 0.82 \cdot 0.26^{1/2}1.91^{1/4}\{\cos[(6/7)10.4°]\}^{1/2} = 0.49$ introduced in Section 3.2 (step 3). Because the geometry of the Lake Askja is not symmetrical, different θ result on the two slide sides. The wavefront length at $r = d_M$ is thus calculated using $\theta_1 = 32.4°$, $\theta_2 = 44.1°$ (Fig. 17) and the slide width $b = 550$ m resulting in $l_w(r' = d_M, \theta) = b + \theta_{rad,1}d_M + \theta_{rad,2}d_M = 550 + 32.4(\pi/180)531 + 44.1(\pi/180)531 = 1259$ m (step 4). Note that r' in Eq. (9) is replaced here with r because the geometry already starts to diverge at $r = 0$ rather than at $r' = 0$. Since H_M applies to 2D, the observed wave height at the coupling location may be smaller due to lateral energy spread. This is taken into account by spreading the wave energy over the wavefront length resulting in $H(r' = 0, \gamma' = 0°, \theta) = H_M(r' = 0, \gamma' = 0°, \theta = 0°)[b/l_w(r' = 0, \theta)]^{1/2} = 43.3(550/1259)^{1/2} = 28.6$ m (step 5).

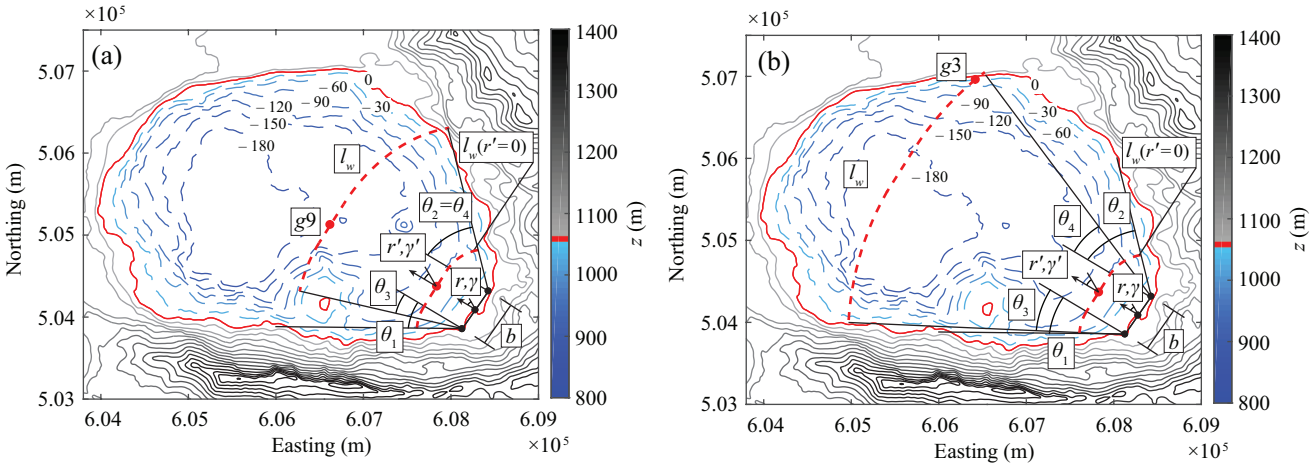

Figure 17: Computation examples for (a) wave gauge 9 and (b) wave gauge 3 of Gylfadóttir et al. (2017). The red line highlights the SWL = 1058 m above sea level. The contours represent a spacing of $\Delta z = 30$ m in global coordinates with dashed lines and solid lines representing the terrain elevation below and above the SWL, respectively.

The wave heights are calculated at wave gauges 9 ($r = 1970$ m, $\gamma = 0°$) and 3 ($r = 3440$ m, $\gamma = 23.7°$) (Gylfadóttir et al., 2017). At gauge 9 the wavefront length, again with r' replaced by r, is $l_w = 550 + 19.2(\pi/180)1970 + 44.1(\pi/180)1970 = 2726$ m by using $\theta_3 = 19.2°$ and $\theta_4 = 44.1°$ (Fig. 17a, step 6). θ_3 is chosen under the consideration of the water body restriction caused by the small island on the left hand side of the slide, which affects the lateral

wave energy spread. Finally, applying Eq. (13) for $\gamma = 0°$ with the pre-factors $\beta = 1.03$ and $\beta_E = 1.27$ (for cnoidal waves, Table 3) results in $H = 20.0$ m and $H = 24.7$ m respectively (step 7). These values are close (-10.0% and $+11.2\%$ difference, respectively) to the wave height $H = 22.2$ m found by Gylfadóttir et al. (2017).

At gauge 3 the wavefront length is $l_w = 3614$ m with $\theta_3 = 30.5°$ and $\theta_4 = 20.5°$ (Fig. 17b). Eq. (13) is applied with $\gamma = 23.7°$ and the pre-factors $\beta = 1.03$ and $\beta_E = 1.27$ (Table 3) resulting in $H = 17.1$ m and $H = 21.0$ m, respectively, which in turn underestimate the wave height of $H = 26.0$ m found by Gylfadóttir et al. (2017) by 34.2% and 19.2%, respectively. However, such an underestimation is expected as gauge 3 is located close to the lake shore where shoaling, which is not considered in Eq. (13), becomes important. Shoaling could also be found in combination with other depth and geometry related effects such as reflection and depth trapping of the tsunami (Bellotti et al., 2012), which in combination with the impact on the coast may alter the tsunami characteristics.

The same procedure is applied to calculate the landslide-tsunami amplitude using Eq. (14). Step 1 and step 2 remain the same as for the wave height. In 3 the maximum wave amplitude $a_M = 4/9\mathrm{P}^{4/5}h = 34.7$ m (Heller and Hager, 2010) instead of H_M. Step 4 remains unchanged and step 5 is updated by calculating the wave amplitude resulting in $a(r' = 0, \gamma' = 0, \theta) = a_M(r' = 0, \gamma' = 0°, \theta = 0°)[b/l_w(r' = 0, \theta)]^{1/2} = 22.9$ m. Step 6 remains unchanged and in step 7 Eq. (14) is used, with $\beta = 0.85$ and $\beta_E = 1.09$ (Table 3). The results for the wave amplitude, together with the ones for the wave heights, are summarised in Table 9. The values are close to $a = 13.4$ m for gauge 9 and $a = 14.2$ m for gauge 3 found by Gylfadóttir et al. (2017).

Table 9: Calculated wave parameters based on Eqs. (13) and (14) compared to the numerically derived parameters by Gylfadóttir et al. (2017). In brackets the values $(y_{pred}/y_{num} - 1) \times 100$ are shown (* values affected by shoaling).

	Predicted H (m)		H (m) (Gylfadóttir et al., 2017)	Predicted a (m)		a (m) (Gylfadóttir et al., 2017)
Pre-factor	β	β_E	-	β	β_E	-
gauge 9	20.0 (-10.0%)	24.7 ($+11.2\%$)	22.2	13.2 (-1.5%)	17.0 ($+26.8\%$)	13.4
gauge 3	17.1 (-34.2%)	21.0 (-19.2%)	26.0*	11.3 (-20.4%)	14.5 ($+2.1\%$)	14.2*

5. Conclusions

This study aimed to enhance the physical understanding of the effect of the water body geometry on wave propagation with particular focus on landslide-tsunamis. This aim was motivated by the very limited understanding of this effect for intermediate geometries between the 2D and 3D geometries. This effect is associated with two components: lateral energy spread caused by the increasing lateral space with the water body side angle θ and frequency dispersion. Idealised water body geometries with increasing $\theta = 0$ (2D), $7.5, 15, 30, 45$ and $90°$(3D) of the flume lateral walls were used to simulate idealised and real

landslide-tsunamis. SWASH, a non-hydrostatic NLSWE model, was used to simulate propagation in the far field, where the wave is reasonable stable. Approximate linear, Stokes, cnoidal and solitary waves were investigated up to a maximum distance of 35 times the water depth from the wave generation zone. These idealised waves in combination with a constant water depth allowed the waves in 2D to be stable and essentially excluded frequency dispersion.

The results in the 3D geometry were validated with diffraction theory given that the wave generated by a landslide shows similarities to a wave diffracted from a wave source of finite width. The wavefront length l_w (Eq. (9)) was found to be an excellent parameter to link the wave heights of the idealised waves in all investigated geometries along the slide axis resulting in a close match with Green's law (Eq. (10)). The wave heights outside the slide axes were also correlated with Green's law, modified with empirical pre-terms. These derived semi-theoretical equations can be used to predict the idealised wave heights and amplitudes in real water bodies based on 2D wave parameters estimated with the method of Heller and Hager (2010).

It was further investigated how well the results derived for idealised waves represent real tsunamis including frequency dispersion. Simulations in the 2D geometry where therefore conducted by using the laboratory landslide-tsunami time series of Heller and Hager (2011). Lateral energy spread is not present in 2D such that the wave decay may essentially be attributed to frequency dispersion. The 2D experiments of Heller and Hager (2011) were compared with SWASH simulations based on experimental time series and idealised waves. An increasing effect of frequency dispersion on wave decay with decreasing wave nonlinearity was observed. This shows that the semi-theoretical equations based on the idealised waves are more appropriate for landslide-tsunamis in proximity of the shallow-water wave regime (solitary-like waves), than for landslide-tsunamis closer to the deep-water regime (Stokes-like waves) (Section 3.2).

The wave decay was also found to increase with θ, especially for solitary waves. In fact, comparing wave heights and amplitudes, the effect of the lateral energy spread is larger in intermediate geometries and 3D than the effect of frequency dispersion in 2D. Finally, a calculation procedure to apply the new semi-theoretical equations to real cases is provided showing a good agreement of the wave heights (up to -10.0%) and amplitudes (up to -1.5%) for the 2014 Lake Askja tsunami.

Given that the findings in this study mainly support initial landslide-tsunami hazard assessment, the effect of frequency dispersion may be neglected for tsunamis in proximity of the shallow-water wave regime (solitary- and cnoidal-like waves). However, in proximity of the deep-water wave regime (Stokes-like waves), frequency dispersion accounts for up to 30% of the wave decay and can not be neglected. The new equations can then still be applied, but will likely result in an over-prediction of the real waves. This may be acceptable for initial landslide-tsunami hazard assessment given that the predicted wave parameters are on the safe side if depth and shore effects are excluded.

Future work will potentially also model the wave generation process and couple the wave propagation model SWASH with a wave generation model. This

would allow to simulate the entire landslide-tsunami process numerically. It is also planned to investigate the effect of a changing bathymetry on tsunamis.

Acknowledgements

The authors would like to thank Prof. Nicholas Dodd for helpful suggestions for this work. Thanks also go to Dr. Sigríður Sif Gylfadóttir and her collaborators for providing their numerical results for the Lake Askja case. The University of Nottingham HPC cluster Minerva has been accessed to perform the numerical simulations.

Notation

A	[-]	= Mathieu function joining factor
a	[L]	= wave amplitude
a_M	[L]	= maximum wave amplitude
a_c	[L]	= wave amplitude at the coupling location
a_l	[L]	= wave amplitude at the last wave gauge
a_t	[L]	= wave trough amplitude
B	[-]	= relative slide width
b	[L]	= slide width at the slide impact location
b'	[L]	= source width at the coupling location
Ce	[-]	= even radial Mathieu function of the first kind
C_r	[-]	= Courant number
c	[L/T]	= wave celerity
ce	[-]	= even angular Mathieu function
c_f	[-]	= bottom friction coefficient
c_g	[L/T]	= wave group celerity
d	[L]	= total water depth
d_M	[L]	= coupling distance
E	[M/T^2]	= mean energy density per unit area
F	[-]	= slide Froude number
Fey	[-]	= even radial Mathieu function of the second kind
g	[L/T^2]	= gravitational acceleration
g_e	[-]	= Mathieu function joining factor
H	[L]	= wave height
H_M	[L]	= maximum wave height
H_c	[L]	= wave height at the coupling location
H_d	[L]	= diffracted wave height
H_i	[L]	= incident wave height
H_l	[L]	= wave height at the last wave gauge
h	[L]	= water depth
I	[-]	= wave intensity
i	[-]	= counter for i-th data sample
Je	[-]	= Mathieu even radial function of the second kind

K'	[-]	= diffraction coefficient
k	[L^{-1}]	= wave number
L	[L]	= wavelength
L_M	[L]	= maximum wavelength
l_s	[L]	= landslide length
l_w	[L]	= wavefront length
M	[-]	= relative slide mass
m	[-]	= integer number
m_s	[M]	= slide mass
N	[-]	= Mathieu function normalising factor
N	[-]	= number of samples
Ne	[-]	= Mathieu even radial function of the first kind
n	[$T/L^{1/3}$]	= Manning's coefficient
n	[-]	= integer number
P	[-]	= impulse product parameter
p_h	[M/LT^2]	= hydrostatic pressure
p_t	[M/LT^2]	= total pressure
q	[M/LT^2]	= non-hydrostatic pressure term
q_d	[-]	= Mathieu function fixed variable
r	[L]	= radial distance from the slide impact
r'	[L]	= radial distance from the coupling location
r_i	[L]	= impact radius
S	[-]	= relative slide thickness
Se	[-]	= Mathieu even angular function
s	[L]	= slide thickness
s_{mat}	[-]	= Mathieu function fixed variable
T	[-]	= wave type product
T	[T]	= wave period
t	[T]	= time from when the slide impacts
t'	[T]	= time from when the wave reaches the coupling location
u	[L/T]	= velocity in x' direction
$\overline{u}$	[L/T]	= depth averaged velocity in x' direction
$\overline{u}_i$	[L/T]	= incident velocity
V_s	[L/T]	= slide velocity
v	[L/T]	= velocity in y' direction
$\overline{v}$	[L/T]	= depth averaged velocity in y' direction
w_b	[L/T]	= velocity at the bottom in z' direction
w_s	[L/T]	= velocity at the surface in z' direction
x	[L]	= x-coordinate from the slide impact
x'	[L]	= x'-coordinate from the coupling location
x_M	[L]	= location of maximum wave amplitude
y'	[L]	= y'-coordinate
y_{num}	[-]	= numerical value
$y_{num,max}$	[-]	= maximum numerical value
$y_{num,min}$	[-]	= minimum numerical value

y_{pred}	[-]	= predicted value
z'	[L]	= z'-coordinate

Greek symbols

α	[°]	= slide impact angle
α_i	[°]	= incident wave angle
β	[−]	= pre-factor in Eqs. (13) and (14) and pre-factor for the best fit
β_E	[−]	= pre-factor in Eqs. (13) and (14) for the upper envelope
γ	[°]	= wave propagation angle from the slide impact
γ'	[°]	= wave propagation angle from the coupling location
γ'_{part}	[°]	= phase angle of the partial wave
ΔH	[L]	= terrain elevation difference
ΔL	[L]	= horizontal distance between two points
$\Delta t'$	[T]	= time difference
Δx	[L]	= distance travelled by the slide above SWL
$\Delta x'$	[L]	= x'-direction grid size and horizontal distance
$\Delta y'$	[L]	= y'-direction grid size
Δz	[L]	= contours spacing in z-direction
$\Delta\gamma'$	[°]	= wave propagation angle difference
$\delta\phi$	[rad]	= angular resolution for Mathieu function
η	[L]	= water surface elevation
η_i	[L]	= incident water surface elevation
θ	[°]	= water body side angle
θ_{rad}	[rad]	= water body side angle in radians
μ	[-]	= effective friction coefficient
ξ	[-]	= elliptic-cylinder coordinates of confocal ellipses
π	[-]	= mathematical constant
ρ_s	[M/L^3]	= slide density
ρ_w	[M/L^3]	= water density
τ	[ML^3/T^2]	= turbulent stress
ϕ	[-]	= elliptic-cylinder coordinates of confocal hyperbolas

Abbreviations

2D	= Wave flume geometry
3D	= Wave basin geometry
CFL	= Courant-Friedrichs-Lewy
CPU	= Central Processing Unit
HPC	= High Performance Computing
MPI	= Message Passing Interface
NLSWE	= Non-Linear Shallow Water Equation
$nRMSE$	= normalised Root Mean Square Error
SPH	= Smoothed Particle Hydrodynamics
SWASH	= Simulating WAves till SHore
SWL	= Still Water Level

A. Symmetry of the numerical solution

Fig. A.1 shows the symmetry of the numerical solution studied with H at $r'/h = 3.0$, 5.0, 10.0, 15.0, 22.5 and 35.0 for the 3D geometry. The H values are calculated using the water surface time series at propagation angles $\gamma' = 0°$ and $\gamma' = \pm 45°$ (Fig. 3f).

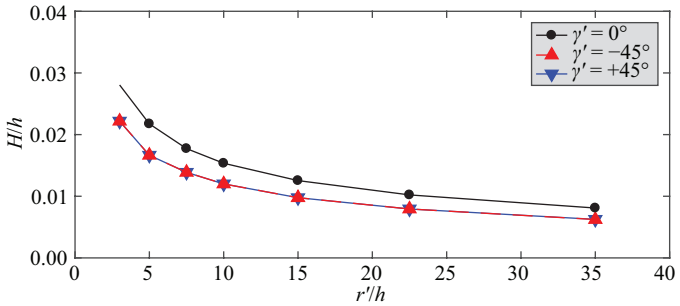

Figure A.1: Symmetry of the numerical solution in the 3D geometry. Relative wave height H/h over the relative radial distance r'/h at $\gamma' = 0°$ and $\gamma' = \pm 45°$.

B. Diffraction theory

The diffraction theory by Carr and Stelzriede (1952) was applied rather than graphical solutions (diffraction diagrams) available in the technical literature for fixed ratios b'/L between the source gap width b' and the wavelength L (e.g. Johnson, 1952; USACE, 1984). This theory was introduced by Morse and Rubenstein (1938) for diffraction of sound and electromagnetic waves at a gap into a infinite plane. This approach has an exact solution for small gaps and defines the energy distribution in function of the wave propagation angle γ'. The solution is based on elliptic-cylinder coordinates defined as

$$\begin{aligned} x' &= b'/2 \cos\xi \cos\phi \\ y' &= b'/2 \sin\xi \sin\phi \end{aligned} \tag{B.1}$$

where ξ are confocal ellipses and ϕ are confocal hyperbolas (Fig. 2 in Carr and Stelzriede, 1952).

For $\phi = 0$ the hyperbolas degenerate in a straight line with a gap of width b'. The three-dimensional wave equation in elliptic-cylinder coordinates is then solved using the Mathieu function (Abramowitz and Stegun, 1964) as a method for variables separation. The solution in function of the energy intensity ratio I (Carr and Stelzriede, 1952; Morse and Rubenstein, 1938) is

$$\begin{aligned} I = \frac{H_d^2}{H_i^2} = \sum_{\mathrm{m,n}} \frac{b'}{L} \frac{4\pi}{\sqrt{s_{mat}}} \frac{1}{N_\mathrm{m} N_\mathrm{n}} \sin\gamma'_{part,\mathrm{m}} \sin\gamma'_{part,\mathrm{n}} Se_\mathrm{m}(s_{mat}, \alpha_i) \cdot \\ \cdot Se_\mathrm{n}(s_{mat}, \alpha_i) Se_\mathrm{m}(s_{mat}, \phi) Se_\mathrm{n}(s_{mat}, \phi) \cos(\gamma'_{part,\mathrm{n}} - \gamma'_{part,\mathrm{m}}) \end{aligned} \tag{B.2}$$

$$I_{r',\phi} = \frac{L}{r'} I \tag{B.3}$$

where Se is the even angular Mathieu function, $s_{mat} = (\pi b'/L)^2$, α_i is the direction of the wave entering the gap (Fig. B.1), ϕ is the angle from the centreline of the gap and r' the radial distance from the source. H_d is the diffracted wave height, H_i the incident wave height and the subscripts m and n are the integer number of the sum terms. Finally, γ'_{part} represents the phase angle of the partial wave and is defined as $\mathrm{ctn}\gamma'_{part} = (Ne_n(s_{mat}, 0)/Je_n(s_{mat}, 0))$ where Ne is the even radial modified Mathieu function of the first kind and Je is the even radial modified Mathieu function of the second kind. Note that in Carr and Stelzriede (1952) the normalising factor $1/(N_\mathrm{m} N_\mathrm{m})$ is missing in their representation of Eq. (B.2).

To solve the Mathieu function the "Mathieu functions toolbox v4.0.6" (Coisson et al., 2016) for Scilab has been used allowing for a high resolution of $\delta\phi = 0.01$ rad in the final solution solving the even angular Mathieu function $ce_n(\phi, q_d)$, the even radial Mathieu function of the first kind $Ce_\mathrm{n}(\phi, q_d)$ and the even radial Mathieu function of the second kind $Fey_n(\phi, q_d)$ where $q_d = s_{mat}/4$. Tabulated values from the National Bureau of Standards (1951) were then used to transform the three precedent solutions with the variables needed to solve the corrected theory of Carr and Stelzriede (1952) resulting in $Se_\mathrm{n}(s_{mat}, \phi) = ce_\mathrm{n}(\phi, q_d)/A_\mathrm{n}$, $Je_n(s_{mat}, \phi) = Ce_\mathrm{n}(\phi, q_d)/A_\mathrm{n} g_{e,\mathrm{n}}$ and $Ne_\mathrm{n}(s_{mat}, \phi) = Fey_\mathrm{n}(\phi, q_d)/A_\mathrm{n} g_{e,\mathrm{n}}$ where A_n and $g_{e,\mathrm{n}}$ are the joining factors.

Fig. B.1 shows the comparison between the calculated solution based on Eq. (B.2) and the diffraction diagram of Pos and Kilner (1987) after Johnson (1952). The $x'-$ and $y'-$axes are normalised with L considering the origin of the reference system at the centre of the breakwater gap. The different contours with each associated value define the wave diffraction coefficient $K' = H_d/H_i = \sqrt{I}$. Other b'/L ratios where investigated with Eq. (B.2) obtaining results with a similar match to the corresponding diffraction diagram (Johnson, 1952) as shown in Fig. B.1. This successfully validated results of the diffraction theory were applied in Fig. 11.

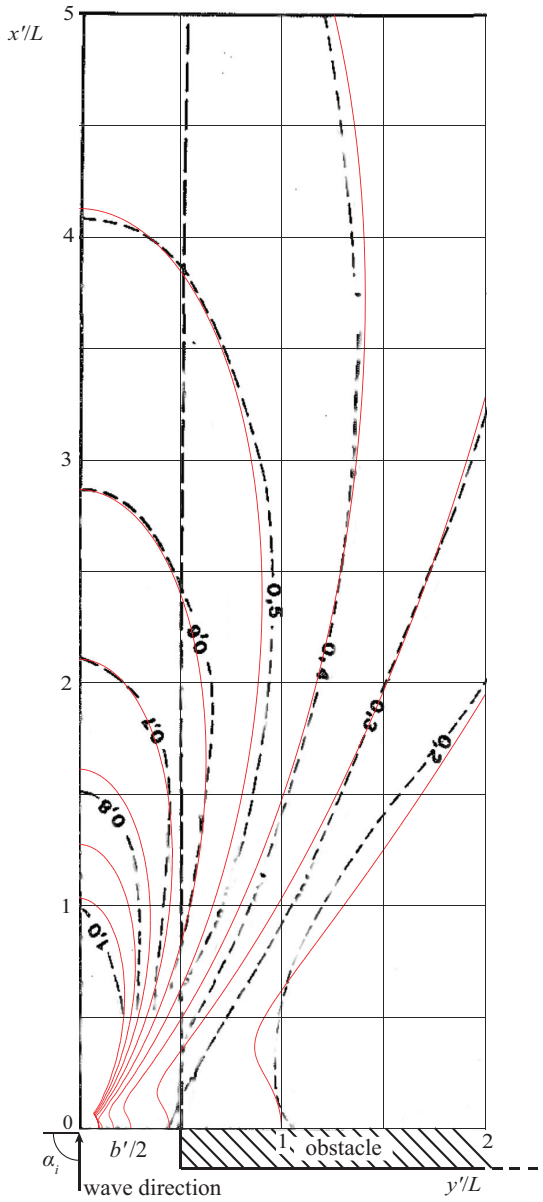

Figure B.1: Comparison of theoretically calculated diffraction solution based on Eq. (B.2) (red line) and graphical solution (diffraction diagrams) of Pos and Kilner (1987) (black dashed line) for $b'/L = 1$ and $\alpha_i = 90°$.

C. Amplitude decay

Table C.1 shows the values of the wavefront length l_w for each wave type. Fig. C.1 shows the wave amplitude decay for each geometry and investigated wave type compared to Green's law (Eq. (12)) based on the wave amplitude a. Finally, Fig. C.2 shows the wave amplitudes for each geometry and wave type compared with Eq. (14).

Table C.1: Wavefront lengths l_w for (a) approximate linear and Stokes waves and (b) cnoidal and solitary waves based on Eq. (9).

(a) Approximate linear and Stokes waves with $h = 0.60$ m

r'/h	2D ($\theta = 0°$)	$\theta = 7.5°$	$\theta = 15°$	$\theta = 30°$	$\theta = 45°$	3D ($\theta = 90°$)
3.0	0.600	1.071	1.543	2.485	3.427	6.255
5.0	0.600	1.385	2.171	3.742	5.312	10.025
7.5	0.600	1.778	2.956	5.312	7.669	14.737
10.0	0.600	2.171	3.742	6.883	10.025	19.450
15.0	0.600	2.956	5.312	10.025	14.737	28.874
22.5	0.600	4.134	7.669	14.737	21.806	43.012
35.0	0.600	6.098	11.596	22.591	35.587	66.573

(b) Cnoidal and solitary waves with $h = 0.30$ m

r'/h	2D ($\theta = 0°$)	$\theta = 7.5°$	$\theta = 15°$	$\theta = 30°$	$\theta = 45°$	3D ($\theta = 90°$)
3.0	0.600	0.836	1.071	1.543	2.014	3.427
5.0	0.600	0.993	1.385	2.171	2.956	5.312
7.5	0.600	1.189	1.778	2.956	4.134	7.669
10.0	0.600	1.385	2.171	3.742	5.312	10.025
15.0	0.600	1.778	2.956	5.312	7.669	14.737
22.5	0.600	2.367	4.134	7.669	11.203	21.806
35.0	0.600	3.349	6.098	11.596	17.093	33.587

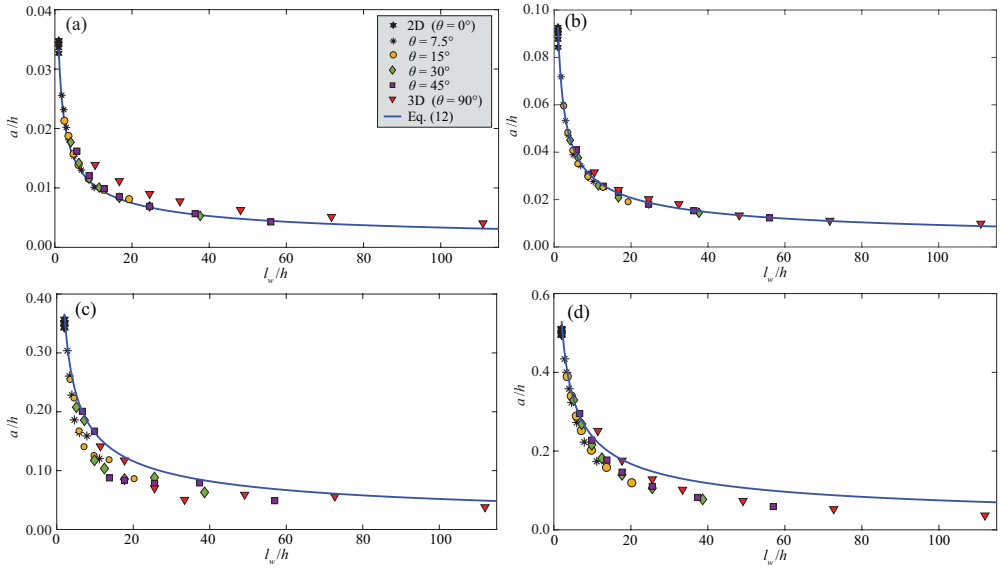

Figure C.1: Wave amplitude decay in all investigated geometries for (a) approximate linear waves, (b) 5^{th} order Stokes waves, (c) 5^{th} order cnoidal waves and (d) 1^{st} order solitary waves compared to Eq. (12).

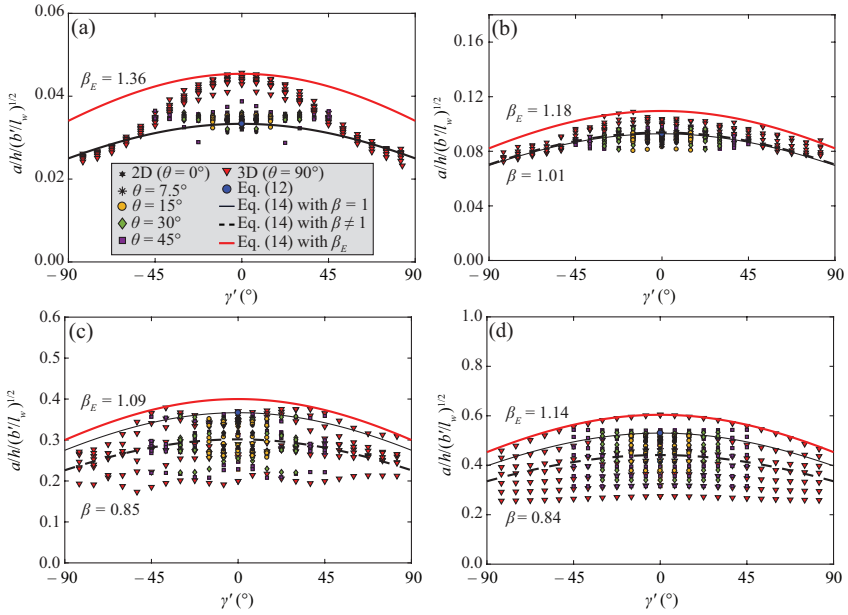

Figure C.2: Lateral wave amplitude decay for (a) approximate linear waves, (b) 5^{th} order Stokes waves, (c) 5^{th} order cnoidal waves and (d) 1^{st} order solitary waves for all investigated geometries, compared to Eq. (14).

D. Lateral spread for approximate linear, cnoidal and solitary waves

The lateral wave decay for the approximate linear, cnoidal and solitary waves is presented here with Fig. D.1 showing the wave heights for the approximate linear waves, Fig. D.2 for cnoidal waves and Fig. D.3 for solitary waves. The cnoidal waves shown in Fig. D.2, especially for $\theta > 15°$ (Fig. D.2c-f), show a convex shape with slightly higher wave heights near the side walls. Although this differs from the trend shown in Fig. 12, similar convex trends were observed in the experiments of Heller et al. (2012). The same convex shape is found for the solitary wave (Fig. D.3d,e) for $\theta = 30°$ and $\theta = 45°$.

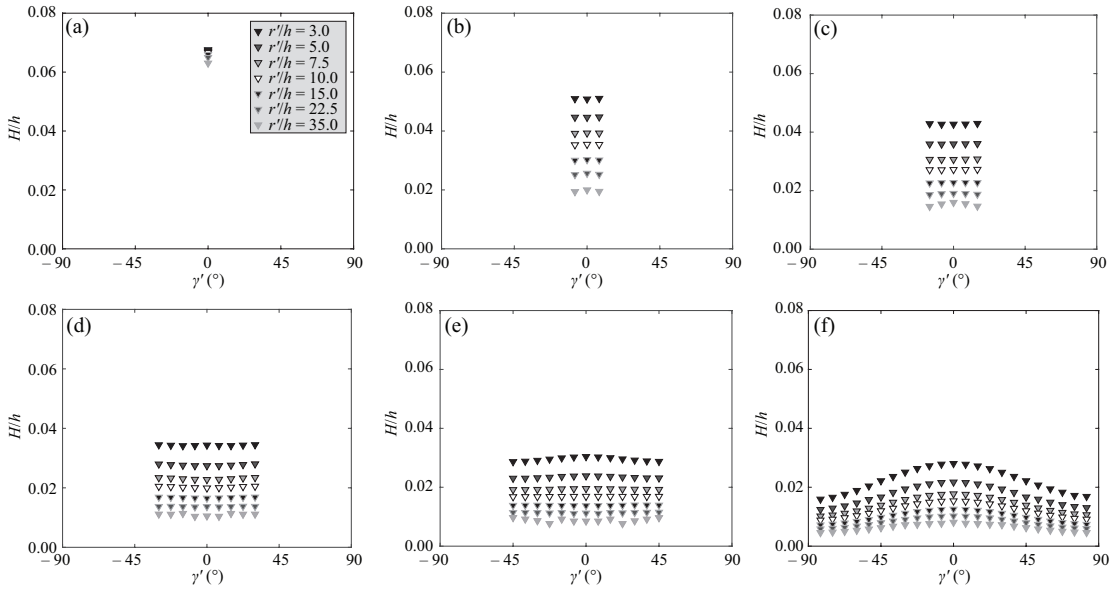

Figure D.1: Relative wave heights H/h for approximate linear waves in intermediated waters as a function of the propagation angle γ' and the relative radial distance r'/h for (a) 2D ($\theta = 0°$), (b) $\theta = 7.5°$, (c) $\theta = 15°$, (d) $\theta = 30°$, (e) $\theta = 45°$ and (f) 3D ($\theta = 90°$).

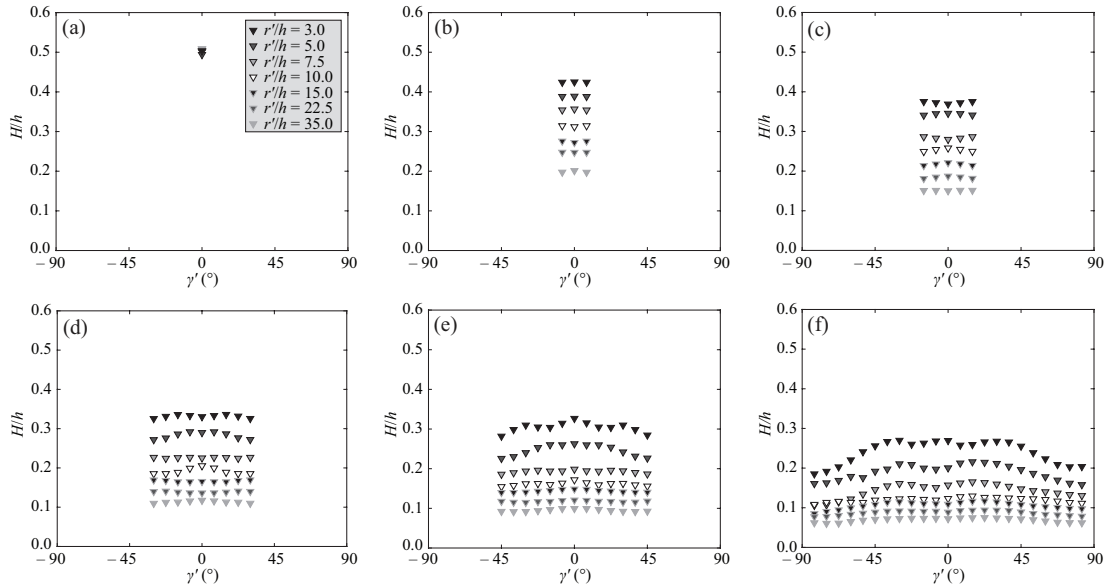

Figure D.2: Relative wave heights H/h for 5^{th} order cnoidal waves as a function of the propagation angle γ' and the relative radial distance r'/h for (a) 2D ($\theta = 0°$), (b) $\theta = 7.5°$, (c) $\theta = 15°$, (d) $\theta = 30°$, (e) $\theta = 45°$ and (f) 3D ($\theta = 90°$).

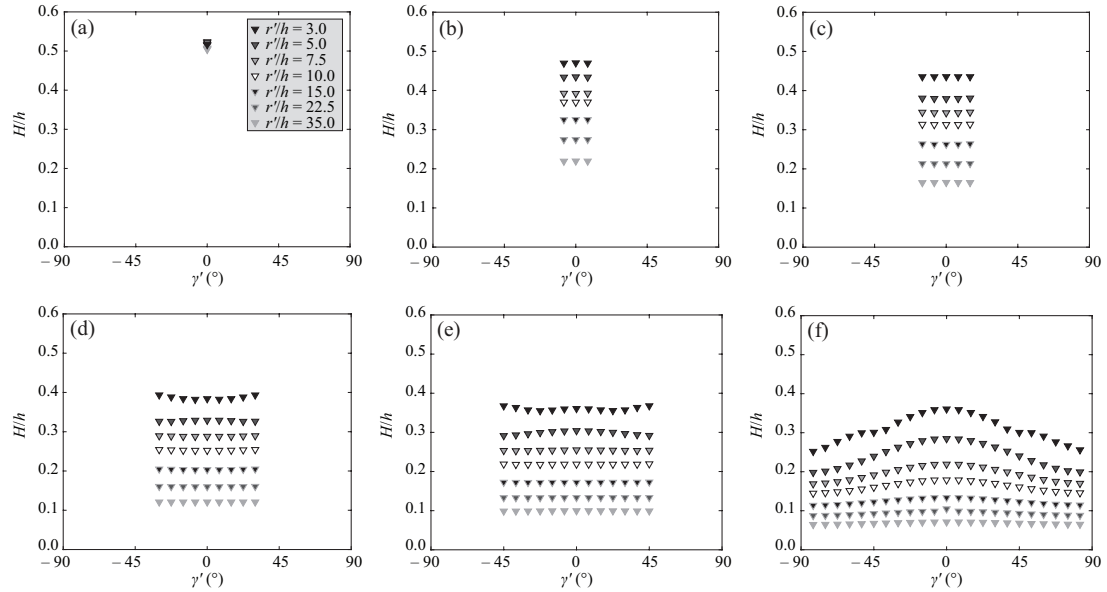

Figure D.3: Relative wave heights H/h for 1^{st} order solitary waves as a function of the propagation angle γ' and the relative radial distance r'/h for (a) 2D ($\theta = 0°$), (b) $\theta = 7.5°$, (c) $\theta = 15°$, (d) $\theta = 30°$, (e) $\theta = 45°$ and (f) 3D ($\theta = 90°$).

References

References

Abadie, S.M., Harris, J.C., Grilli, S.T., Fabre, R., 2012. Numerical modeling of tsunami waves generated by the flank collapse of the Cumbre Vieja Volcano (La Palma, Canary Islands): Tsunami source and near field effects. *Journal of Geophysical Research: Oceans* 117(C05030).

Abramowitz, M., Stegun, I.A., 1964. Handbook of mathematical functions: With formulas, graphs, and mathematical tables. Volume 55. Courier Corporation.

Altomare, C., Domínguez, J.M., Crespo, A.J.C., Suzuki, T., Caceres, I., Gómez-Gesteira, M., 2015. Hybridization of the wave propagation model SWASH and the meshfree particle method SPH for real coastal applications. *Coastal Engineering Journal* 57(4), 1550024–1.

Bellotti, G., Briganti, R., Beltrami, G., 2012. The combined role of bay and shelf modes in tsunami amplification along the coast. *Journal of Geophysical Research: Oceans* 117(8), 1–13.

Blayo, E., Debreu, L., 2005. Revisiting open boundary conditions from the point of view of characteristic variables. *Ocean Modelling* 9(3), 231–252.

Boussinesq, J., 1872. Théorie des ondes et des remous qui se propagent le long d'un canal rectangulaire horizontal, en communiquant an liquide contenu dans ce canal de vitesses sensiblement pareilles de la surface anfond, liouvilles. *Journal de Mathématiques Pures et Appliquées* 17, 55–108.

Brühl, M., Becker, M., 2018. Analysis of subaerial landslide data using non-linear Fourier transform based on Korteweg-deVries equation (KdV-NLFT). *Journal of Earthquake and Tsunami* 12(02), 1840002.

Carr, J.H., Stelzriede, M.E., 1952. Diffraction of water waves by breakwaters. *Gravity Waves, Circular No. 521, U.S. National Bureau of Standards* 109–125.

Chang, P., Melville, W.K., Miles, J.W., 1979. On the evolution of a solitary wave in a gradually varying channel. *Journal of Fluid Mechanics* 95(3), 401–414.

Coisson, R., Vernizzi, G., Yang, X.K., Strelkov, N.O., Baudin, M., 2016. Mathieu functions toolbox v4.0.6. URL: `http://forge.scilab.org/index.php/p/mathieu/` (accessed 21.05.2019).

Couston, L.A., Mei, C., Alam, M.R., 2015. Landslide tsunamis in lakes. *Journal of Fluid Mechanics* 772, 784–804.

Dean, R.G., Dalrymple, R.A., 1991. Water wave mechanics for engineers and scientists. Volume 2. World Scientific, Singapore.

Deltares, 2018. Delft 3D modelling guidelines. URL: `https://publicwiki.deltares.nl/display/D3DGUIDE/Computational+grid` (accessed 21.05.2019).

Dingemans, M.W., 1997. Water wave propagation over uneven bottoms: Part 1. World Scientific, Singapore.

Evers, F.M., Hager, W.H., Boes, R.M., 2019. Spatial impulse wave generation and propagation. *Journal of Waterway, Port, Coastal, and Ocean Engineering* 145(3), 04019011.

Fenton, J.D., 1985. A fifth-order Stokes theory for steady waves. *Journal of Waterway, Port, Coastal, and Ocean Engineering* 111(2), 216–234.

Fenton, J.D., 1999. The cnoidal theory of water waves, *in: Developments in Offshore Engineering*. Elsevier, pp. 55–100.

Fuchs, H., Boes, R., 2010. Berechnung felsrutschinduzierter Impulswellen im Vierwaldstättersee. *Wasser, Energie, Luft* 102(3), 215–221 (in German).

Fuchs, H., Pfister, M., Boes, R., Perzlmaier, S., Reindl, R., 2011. Impulswellen infolge Lawineneinstoss in den Speicher Kühtai. *Wasserwirtschaft* 101(1/2), 54–60 (in German).

Green, G., 1838. On the motion of waves in a variable canal of small depth and width. *Transactions of the Cambridge Philosophical Society* 6, 456–462.

Gylfadóttir, S.S., Kim, J., Helgason, J.K., Brynjólfsson, S., Höskuldsson, Á., Jóhannesson, T., Harbitz, C.B., Løvholt, F., 2017. The 2014 Lake Askja rockslide induced tsunami: Optimization of numerical tsunami model using observed data. *Journal of Geophysical Research: Oceans* 122(5), 4110–4122.

Harbitz, C.B., Glimsdal, S., Løvholt, F., Kveldsvik, V., Pedersen, G.K., Jensen, A., 2014. Rockslide tsunamis in complex fjords: From an unstable rock slope at Åkerneset to tsunami risk in western Norway. *Coastal Engineering* 88, 101–122.

Heller, V., 2011. Scale effects in physical hydraulic engineering models. *Journal of Hydraulic Research* 49(3), 293–306.

Heller, V., Bruggemann, M., Spinneken, J., Rogers, B.D., 2016. Composite modelling of subaerial landslide-tsunamis in different water body geometries and novel insight into slide and wave kinematics. *Coastal Engineering* 109, 20–41.

Heller, V., Hager, W.H., 2010. Impulse product parameter in landslide generated impulse waves. *Journal of Waterway, Port, Coastal, and Ocean Engineering* 136(3), 145–155.

Heller, V., Hager, W.H., 2011. Wave types of landslide generated impulse waves. *Ocean Engineering* 38(4), 630–640.

Heller, V., Hager, W.H., Minor, H.-E., 2008. Scale effects in subaerial landslide generated impulse waves. *Experiments in Fluids* 44(5), 691–703.

Heller, V., Hager, W.H., Minor, H.-E., 2009. Landslide generated impulse waves in reservoirs: Basics and computation. R. Boes, ed. ETH Zurich, Zurich.

Heller, V., Moalemi, M., Kinnear, R.D., Adams, R.A., 2012. Geometrical effects on landslide-generated tsunamis. *Journal of Waterway, Port, Coastal, and Ocean Engineering* 138(4), 286–298.

Heller, V., Spinneken, J., 2013. Improved landslide-tsunami prediction: Effects of block model parameters and slide model. *Journal of Geophysical Research: Oceans* 118(3), 1489–1507.

Heller, V., Spinneken, J., 2015. On the effect of the water body geometry on landslide-tsunamis: Physical insight from laboratory tests and 2D to 3D wave parameter transformation. *Coastal Engineering* 104, 113–134.

Huber, A., 1980. Schwallwellen in Seen als Folge von Felsstürzen. Ph.D. thesis. ETH Zurich, Zurich (in German).

Huber, A., Hager, W.H., 1997. Forecasting impulse waves in reservoirs. *Transactions of the International Congress on Large Dams* 1, 993–1006.

Jiang, L., LeBlond, P.H., 1994. Three-dimensional modeling of tsunami generation due to a submarine mudslide. *Journal of Physical Oceanography* 24(3), 559–572.

Johnson, J.W., 1952. Engineering aspects of diffraction and refraction. *Proceedings of the American Society of Civil Engineers* 78(3), 1–32.

Körner, H.J., 1976. Reichweite und Geschwindigkeit von Bergstürzen und Fließschneelawinen. *Rock Mechanics* 8(4), 225–256 (in German).

Kranzer, H.C., Keller, J.B., 1959. Water waves produced by explosions. *Journal of Applied Physics* 30(3), 398–407.

Lamb, H., 1945. Hydrodynamics. Dover Publications, New York.

Liu, J., Zang, C., Tian, S., Liu, J., Yang, H., Jia, S., You, L., Liu, B., Zhang, M., 2013. Water conservancy projects in China: Achievements, challenges and way forward. *Global Environmental Change* 23(3), 633–643.

Liu, P.L.F., Wu, T.R., Raichlen, F., Synolakis, C., Borrero, J., 2005. Runup and rundown generated by three-dimensional sliding masses. *Journal of Fluid Mechanics* 536, 107–144.

Ma, G., Shi, F., Kirby, J.T., 2012. Shock-capturing non-hydrostatic model for fully dispersive surface wave processes. *Ocean Modelling* 43, 22–35.

Morse, P.M., Rubenstein, P.J., 1938. The diffraction of waves by ribbons and by slits. *Physical Review Letters* 54(11), 895–898.

Mulligan, R.P., Take, A.W., 2017. On the transfer of momentum from a granular landslide to a water wave. *Coastal Engineering* 125, 16–22.

National Bureau of Standards, U.S., 1951. Tables relating to Mathieu functions. Columbia University Press, New York.

Panizzo, A., De Girolamo, P., Petaccia, A., 2005. Forecasting impulse waves generated by subaerial landslides. *Journal of Geophysical Research: Oceans* 110(C12), 1–23.

Penney, W.G., Price, A.T., Martin, J.C., Moyce, W.J., Thornhill, C.K., 1952. Part I. the diffraction theory of sea waves and the shelter afforded by breakwaters. *Philosophical Transactions of the Royal Society London A* 244(882), 236–253.

Pos, J.D., Kilner, F.A., 1987. Breakwater gap wave diffraction: An experimental and numerical study. *Journal of Waterway, Port, Coastal, and Ocean Engineering* 113(1), 1–21.

Pudasaini, S.P., Miller, S.A., 2013. The hypermobility of huge landslides and avalanches. *Engineering Geology* 157, 124–132.

Roelvink, D., Reniers, A., Van Dongeren, A., Van Thiel de Vries, J., Lescinski, J., McCall, R., 2010. Xbeach model description and manual. *Unesco-IHE Institute for Water Education, Deltares and Delft University of Technology. Report June* 21, 2010.

Romano, A., Bellotti, G., Di Risio, M., 2013. Wavenumber-frequency analysis of the landslide-generated tsunamis at a conical island. *Coastal Engineering* 81, 32–43.

Ruffini, G., Briganti, R., Alsina, J.M., Brocchini, M., Dodd, N., McCall, R., 2019. Numerical modelling of flow and bed evolution of bi-chromatic wave groups on an intermediate beach using non-hydrostatic XBeach. *Journal of Waterway, Port, Coastal, and Ocean Engineering* (in press).

Shi, F., Kirby, J.T., Harris, J.C., Geiman, J.D., Grilli, S.T., 2012. A high-order adaptive time-stepping TVD solver for Boussinesq modeling of breaking waves and coastal inundation. *Ocean Modelling* 43, 36–51.

Slingerland, R.L., Voight, B., 1979. Occurrences, properties, and predictive models of landslide-generated water waves. *Developments in Geotechnical Engineering* 14, 317–394.

Stelling, G., Duinmeijer, S.P.A., 2003. A staggered conservative scheme for every Froude number in rapidly varied shallow water flows. *International Journal for Numerical Methods in Fluids* 43(12), 1329–1354.

Stelling, G., Zijlema, M., 2003. An accurate and efficient finite-difference algorithm for non-hydrostatic free-surface flow with application to wave propagation. *International Journal for Numerical Methods in Fluids* 43(1), 1–23.

SWASH, T., 2016. SWASH - User manual Version 4.01. Delft University of Technology, Environmental Fluid Mechanics Section.

Synolakis, C.E., Bardet, J.P., Borrero, J.C., Davies, H.L., Okal, E.A., Silver, E.A., Sweet, S., Tappin, D.R., 2002. The slump origin of the 1998 Papua New Guinea tsunami 458(2020), 763–789.

Tan, H., Ruffini, G., Heller, V., Chen, S., 2018. A numerical landslide-tsunami hazard assessment technique applied on hypothetical scenarios at Es Vedrà, offshore Ibiza. *Journal of Marine Science and Engineering* 6(4), 1–22.

USACE, 1984. Shore protection manual. *Army Engineer Waterways Experiment Station, Vicksburg, MS. 2v:* 93–99.

van Vledder, G.P., Zijlema, M., 2014. Non-hydrostatic wave modeling in partly sheltered harbor basins. *Coastal Engineering Proceedings* 1(34), 11.

Watt, S.F.L., Talling, P.J., Vardy, M.E., Heller, V., Hühnerbach, V., Urlaub, M., Sarkar, S., Masson, D.G., Henstock, T.J., Minshull, T.A., Paulatto, M., Le Friant, A., Lebas, E., Berndt, C., Crutchley, G.J., Karstens, J., Stinton, A.J., Maeno, F., 2012. Combinations of volcanic-flank and seafloor-sediment failure offshore Montserrat, and their implications for tsunami generation. *Earth and Planetary Science Letters* 319, 228–240.

Watts, P., Grilli, S.T., Tappin, D.R., Fryer, G.J., 2005. Tsunami generation by submarine mass failure. ii: Predictive equations and case studies. *Journal of Waterway, Port, Coastal, and Ocean Engineering* 131(6), 298–310.

Wiegel, R.L., Noda, E.K., Kuba, E.M., Gee, D.M., Tornberg, G.F., 1970. Water waves generated by landslides in reservoirs. *Journal of the Waterways, Harbors and Coastal Engineering Division* 96(2), 307–333.

Wikipedia, 2018. URL: `https://en.wikipedia.org/wiki/List_of_Norwegian_fjords` (accessed 21.05.2019).

Winckler, P., Liu, P.L.F., 2015. Long waves in a straight channel with non-uniform cross-section. *Journal of Fluid Mechanics* 770, 156–188.

Zijlema, M., Stelling, G., 2005. Further experiences with computing non-hydrostatic free-surface flows involving water waves. *International Journal for Numerical Methods in Fluids* 48(2), 169–197.

Zijlema, M., Stelling, G., Smit, P., 2011. SWASH: An operational public domain code for simulating wave fields and rapidly varied flows in coastal waters. *Coastal Engineering* 58(10), 992–1012.

Zitti, G., Ancey, C., Postacchini, M., Brocchini, M., 2016. Impulse waves generated by snow avalanches: Momentum and energy transfer to a water body. *Journal of Geophysical Research: Earth Surface* 121(12), 2399–2423.